J. Fluid Mech. (2005), *vol.* 545, *pp.* 213–243.
doi:10.1017/S0022112005006439 Printed in the United Kingdom

Linear and nonlinear convection in solidifying ternary alloys

By D. M. ANDERSON[1] AND T. P. SCHULZE[2]

[1]Department of Mathematical Sciences, George Mason University, Fairfax, VA 22030, USA
[2]Department of Mathematics, University of Tennessee, Knoxville, TN 37996-1300, USA

(Received 3 June 2004 and in revised form 9 May 2005)

In this paper we consider buoyancy-driven flow and directional solidification of a ternary alloy in two dimensions. A steady flow can be established by forcing liquid downward at an average rate V through a temperature gradient that is fixed in the laboratory frame of reference and spans both the eutectic and liquidus temperature of the material being solidified. Our results include both a linear stability analysis and numerical solution of the governing equations for finite-amplitude steady states. The ternary system is characterized by two distinct mushy zones – a primary layer with dendrites composed of a single species and, beneath the primary layer, a secondary layer with a dendritic region composed of two species. The two layers have independent effective Rayleigh numbers, which allows for a variety of convection scenarios.

1. Introduction

While convection during the solidification of binary alloys has been the focus of attention for a number of years (for reviews see Worster 1997, 2000; Davis 2001), investigation of multi-component materials is a more recent development. The interest in multi-component alloys stems from both the relevance to metallurgy and geophysics and from the emergence of new phenomena in these more complicated systems.

In this paper, we aim to explore convection in mushy layers with substructure due to the presence of three species. Invariably, this structure emerges as the result of one material solidifying or precipitating at higher temperatures than the other two. Under typical growth conditions, the resulting interface is highly unstable and leads rapidly to the formation of a layer of dendrites. Upon further cooling, a second dendritic layer composed of two solid species begins to form. Finally, upon being cooled below the ternary eutectic temperature, all three species completely solidify. This double mushy layer geometry was identified experimentally by Aitta, Huppert & Worster (2001*a*, *b*) in the aqueous ternary system water–potassium nitrate–sodium nitrate (H_2O–KNO_3–$NaNO_3$). Aitta *et al.* and Anderson (2003) speculated on the possible convective behaviour in this system. In particular, the following four configurations were anticipated: both mushy layers are convectively unstable, only the primary mushy layer is unstable, only the secondary mushy layer is unstable, and both mushy layers are stable.

Experimental work by Thompson *et al.* (2003*b*) on the aqueous ternary system H_2O–KNO_3–$NaNO_3$ described a convection scenario in which the primary mushy layer was unstable and the secondary mushy layer was stable and non-convective. In these experiments, convection in the primary and liquid layers reduced the unstable concentration gradient and, after a transient period of convection, the growth of the

secondary mushy layer overtook the primary layer and the system underwent a transition to a non-convecting state. These authors also developed a global conservation model to describe the system in this regime and were able to obtain good agreement with the experimentally observed growth characteristics by incorporating into the model the measured heat and solute fluxes. Another related experimental system, examined by Bloomfield & Huppert (2003), is the aqueous system H_2O–$CuSO_4$–Na_2SO_4. These authors assessed regimes of thermal and compositional buoyancy for a configuration in which the system was cooled on the side.

A number of diverse models have been used to study ternary alloys, with differences that are dictated in large part by the complexity of the equilibrium phase diagram under consideration. Krane, Incropera & Gaskell (1997) have developed a ternary alloy model and have performed two- and three-dimensional simulations of convective patterns and macrosegregation for the ternary alloy lead–antimony–tin (Pb–Sb–Sn) (Krane & Incropera 1997; Krane, Incropera & Gaskell 1998). Felicelli, Poirier & Heinrich (1997, 1998) have performed simulations for selected ternary and quaternary alloys in two and three dimensions. Computations of micro- and macrosegregation in nickel-based superalloys and the associated mushy-layer evolution that incorporate a phase equilibrium subroutine for nickel-based superalloys (Boettinger *et al.* 1995) have been performed by Schneider *et al.* (1997). Beckermann, Gu & Boettinger *et al.* (2000) described experiments and computations in which a single Rayleigh number was used to characterize and predict chimney convection in nickel-based superalloys. The aqueous ternary system considered by Aitta *et al.* (2001*a*,*b*) is notable in the company of its metallurgical counterparts in that the underlying ternary phase diagram is readily defined by only a small number of simple expressions (for details see next section). The simplicity of the phase diagram for this system, as well as the potential for further laboratory experiments, has encouraged a number of recent investigations. Anderson (2003) developed a model for diffusion-controlled (non-convecting) solidification of a ternary alloy and identified similarity solutions for solidification from a cooled boundary. Thompson, Huppert & Worster (2003*a*) developed a related model based on global conservation arguments. In both of these papers, a detailed characterization of the non-convecting states was given. We shall make use of this relatively simple phase diagram in the present paper so that our focus can be directed toward the convective phenomena occurring in the system.

Following a well-established tradition of binary solidification work, we shall consider a 'crystal pulling' configuration, also known as 'directional' solidification. The idea is to force material at a uniform mass flux through a temperature gradient that is fixed in a laboratory frame of reference. Linear stability analyses (Worster 1992; Chen, Lu & Yang 1994; Emms & Fowler 1994; Anderson & Worster 1996), weakly nonlinear analyses (Amberg & Homsy 1993; Anderson & Worster 1995; Chung & Chen 2000; Riahi 2002) and nonlinear studies (Schulze & Worster 1998, 1999, 2001; Chung & Worster 2002) of directional solidification of convecting binary alloys have been carefully investigated. Among these, the linear stability analysis of Worster (1992) and the nonlinear study of Schulze & Worster (1999) are closely related to the present study.

For the case of ternary alloys, the most closely related study is that of Anderson (2003), who examined the similarity solution for non-convecting solidification from a fixed cold boundary. Much of the intuition gained from the previous work on ternary alloys can be applied here, but the present configuration differs from that examined by Anderson in that here, non-convecting solutions can be expressed independently of time (in a moving frame), and hence are well-suited for stability analyses. We shall

explore both the linear stability of this system with respect to solutal convection and the nonlinear behaviour of the system by computational means.

Some of the results we describe here can be compared with previous work by McKibbin & O'Sullivan (1980, 1981), who considered the onset and nonlinear development of convection in a layered porous medium heated from below in a box of finite width. They described two- and three-layer systems in which individual layer thicknesses and permeabilities were prescribed independently. A temperature gradient was imposed across the entire system and either a constant pressure or zero mass flux condition was imposed at the upper boundary. Their results included the following observations: (i) onset of convection tends to be similar to that of a homogeneous system if the permeability contrast between layers is not large, (ii) permeability contrast between layers can lead to localization of convection in a higher permeability layer, (iii) localization of the flow in a relatively thin layer tends to increase the critical Rayleigh number and increase the wavenumber of the flow pattern, and (iv) critical Rayleigh numbers for an impermeable top boundary are larger than those for the constant-pressure top boundary. Nield & Bejan (1999) summarize a number of other related calculations on convection in layered porous media.

There are several important differences between the layered systems with constant permeabilities, just described, and the present work. (i) The concentration, rather than thermal, gradients control the onset and nature of convection and there are two independent Rayleigh numbers that characterize the system. (ii) Base state properties such as the mushy-layer thicknesses and non-uniform permeability profiles, which may vary broadly from one base state to the next, also play a major role. (iii) The interfaces are free boundaries in our analysis and may evolve to highly nonlinear states. (iv) The present porous layers are reactive: the solid fraction, and hence permeability, varies in space and time and the convection under consideration leads generally to local dissolution or additional growth of solid. Some of the consequences of this evolving structure, which we address further below, are the formations of inclusions in the primary and secondary mushy layers in the ternary alloy system.

Our paper is organized as follows. In § 2, we briefly review the ternary phase diagram and describe the governing equations. In § 3, we identify the basic state solution and investigate its stability. In § 4, we describe the numerical techniques used to find nonlinear steady states. In § 5, we describe the results, both linear and nonlinear, arrived at by these methods. In § 6, we present our conclusions.

2. Formulation

2.1. *Ternary phase diagram*

The ternary phase diagram identifies the equilibrium phase of a material at a given temperature and composition. The simplified ternary phase diagram we consider here is the same as that used by Anderson (2003) and is loosely based on the experimental system H_2O–KNO_3–$NaNO_3$ considered by Aitta *et al.* (2001*a*); this follows the more general description of Smallman (1985). The phase diagram we consider makes use of two simplifying assumptions: there are no solid solutions – that is, complete immiscibility in the solid phases, and there exist linear relations between temperature and compositions along the liquidus surface and cotectic lines. Both of these assumptions are more representative of aqueous solutions than of metallic systems, which tend to have extremely complicated phase diagrams. The first assumption provides an important simplification in that the amount of material released upon re-dissolution can be ascertained from the local solid fraction(s) without knowledge of the

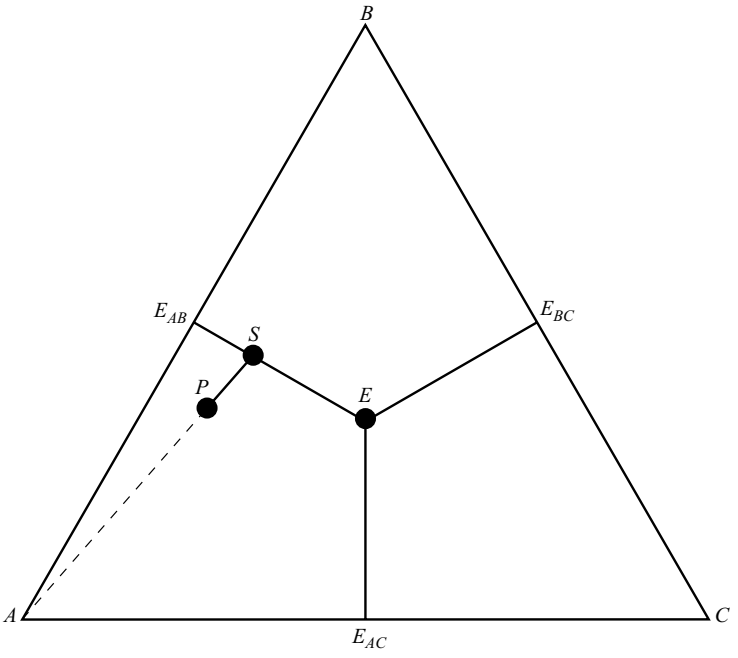

FIGURE 1. A projection of a ternary phase diagram onto the base-plane, where species compositions are indicated by the convention described in the text. The labelled points P, S and E correspond to the state of the system at the primary, secondary and eutectic fronts.

thermodynamic conditions under which the material was solidified, i.e. the system does not exhibit a history-dependence. The second assumption will provide a simple relationship between liquid compositions and the temperature when an additional assumption of local equilibrium is invoked below.

In a full ternary phase diagram, the coordinates in a triangular base indicate the composition while an axis orthogonal to this base represents the temperature. Figure 1 shows the compositional axes in the phase diagram under consideration. We denote the liquid compositions of components A, B and C by A, B and C, which are typically measured in wt % and are normalized here so that $A + B + C = 1$, and the temperature by T. The three corners correspond to the pure materials A, B and C. Each side represents the composition associated with a binary eutectic phase diagram. For example, the A–B side has $C = 0$ and the point marked E_{AB} corresponds to the binary eutectic point of the A–B system. Along each side of the ternary phase diagram, cotectic curves extend from the binary eutectic points into the interior of the phase diagram and demark boundaries of three liquidus surfaces. The three cotectic curves join together at the ternary eutectic point where the temperature is T_E and the compositions are A_E, B_E and C_E. The temperatures along the liquidus surface and cotectic boundary are specified below in terms of the composition.

A material element moving with the liquid through the primary and secondary mushy layers can be identified with a solidification path in the ternary phase diagram. Consider a liquid phase ternary alloy that upon cooling reaches the point P (see figure 1) on a liquidus surface. Upon further cooling, solid A, composed of pure A, solidifies to form the dendritic solid in the primary mushy layer while the components B and C are rejected into the residual liquid. The result of this is an increase of

component B and C in the liquid and corresponds to a path which descends along the liquidus surface toward point S on the cotectic curve. In the absence of flow and solute diffusion, this path corresponds to a 'tie-line', along which the ratio of B and C remains fixed. In the present study, although flow is considered, we find that the tie-line constraint can still be applied (see § 2.2) (Further evidence supporting the tie-line condition follows from the experimental measurements reported by Aitta *et al.* (2001*a*, *b*) for diffusion limited regimes and by Thompson *et al.* (2003*b*) for convective regimes; both references show clearly that the liquid compositions in the primary mushy layer follow a tie-line to a very good approximation.) Once the cotectic boundary is reached at point S, solidification continues with solid A (pure A) and solid B (pure B) forming the dendritic solid of the secondary mushy layer. In the secondary mushy layer the liquid compositions follow the cotectic curve toward the ternary eutectic point (point E). At the eutectic point, the remaining liquid solidifies to form a eutectic solid composed of solids A, B and C. We denote the local volume fraction of solids A, B and C by ϕ_A, ϕ_B and ϕ_C, the total solid fraction by $\phi = \phi_A + \phi_B + \phi_C$ and the liquid fraction by $\chi = 1 - \phi$.

The calculations described in the present paper require the definition of only one liquidus surface and cotectic boundary and so, without loss of generality, we focus on the liquidus surface associated with corner A and the cotectic line associated with the A–B side of the phase diagram. We express these conditions in terms of a dimensionless temperature $\tilde{T} = (T - T^P)/\Delta T$, where $\Delta T = T^P - T^E$ is the temperature difference across both mushy layers defined in terms of the temperature at the primary mushy layer front T^P and the temperature at the eutectic front T^E. This implies that the dimensionless temperature at the primary mushy layer front is zero and the dimensionless eutectic temperature is -1. We define the liquidus surface by the equation

$$T^{\mathscr{L}}(A, B) = -1 + M_A(A - A^E) + M_B(B - B^E), \tag{2.1}$$

and the cotectic line by the two equations

$$A = A^{\mathscr{C}}(T) = A^E + \frac{1}{M_A^{\mathscr{C}}}(T + 1)\ ,\ B = B^{\mathscr{C}}(T) = B^E + \frac{1}{M_B^{\mathscr{C}}}(T + 1). \tag{2.2}$$

The quantities M_A, M_B, $M_A^{\mathscr{C}}$ and $M_B^{\mathscr{C}}$ represent the various liquidus and cotectic slopes, made dimensionless with respect to the temperature difference ΔT, whose values can be given in terms of three points on the liquidus surface and cotectic line; we use point P (where $T = 0$), point E_{AB} (where $T = T^{AB}$) and point E (where $T = -1$). Requiring that point P lies on the liquidus surface leads to

$$1 = M_A(A^P - A^E) + M_B(B^P - B^E). \tag{2.3}$$

Requiring that the cotectic line pass through the binary eutectic point E_{AB} leads to

$$M_A^C = \frac{T^{AB} + 1}{A^{AB} - A^E}, \quad M_B^C = \frac{T^{AB} + 1}{B^{AB} - B^E}, \tag{2.4}$$

where T^{AB}, A^{AB} and B^{AB} are the values of dimensionless temperature T and compositions A and B at the binary eutectic point E_{AB}. A fourth relation follows from substituting (2.2) into (2.1); this recognizes that the cotectic line is part of the liquidus surface:

$$1 = \frac{M_A}{M_A^{\mathscr{C}}} + \frac{M_B}{M_B^{\mathscr{C}}}. \tag{2.5}$$

We shall consider a compositionally-symmetric ternary phase diagram where $A^E = B^E = 1/3$, $A^{AB} = B^{AB} = 1/2$, $A^{AC} = 1/2$ and $B^{AC} = 0$. If we consider symmetry with respect to temperature, the binary eutectic temperatures on the A–B and A–C sides of the phase diagram are equal, $T^{AB} = T^{AC}$, and the equations above can be simplified further, provided a special choice for T^{AB} is made. In the fully symmetric case, then, we find that $M_B = 0$, $M_A = M_A^{\mathscr{C}} = M_B^{\mathscr{C}} = 1/(A^P - 1/3)$ and that $T^{AB} = -1 + M_A/6$. That a specific value of T^{AB} is required for symmetry reflects the fact that while we use three points to specify the liquidus plane, an additional constraint at a fourth point on the plane (the temperature at the A–C binary eutectic) is applied to maintain symmetry.

2.2. *Governing equations*

In this paper, we consider the two-dimensional flow and directional solidification of a ternary alloy in the region $0 < z < H$. This region contains three layers: a liquid layer in $h^P < z < H$, a primary mushy layer in $h^S < z < h^P$ and a secondary mushy layer in $0 < z < h^S$. A steady flow can be established within this domain by forcing liquid downward at an average rate V through a temperature gradient that is fixed in the laboratory frame of reference and spans both the eutectic and liquidus temperature of the material being solidified. We shall assume there is no latent heat released upon solidification, there is no solute diffusion, there is no density change upon solidification, the system is in local equilibrium so that the temperature and species concentrations are coupled through the liquidus surface and cotectic line in the equilibrium phase diagram, and that the thermal properties are constant and equal for all species and phases. Further, we assume the liquid density depends linearly on temperature and composition

$$\rho = \rho_0(1 + \alpha(T - T^P) + \beta_A A + \beta_B B),$$

where ρ_0 is a reference density, α is a thermal expansion coefficient, and β_A and β_B model the change in density with species composition. Finally, we employ the Boussinesq approximation.

In addition to the thermodynamic variables defined above, we decompose the fluid motion into a portion due to the uniform translation of the system, $-V\hat{\boldsymbol{k}}$, and a flux driven by buoyancy $\boldsymbol{u}$. Since we have subtracted the uniform motion of the solid phase, this buoyancy-driven flux is also the Darcy flux – the flux of fluid with respect to a stationary solid phase. In the liquid, $\boldsymbol{u}$ reduces to the portion of the fluid velocity driven by buoyancy. We shall represent this quantity using a streamfunction so that $\boldsymbol{u} = \{-\psi_z, \psi_x\} = \nabla \times (\psi \hat{j})$. Thus, in the absence of convection, we will have $\boldsymbol{u} = 0$, which corresponds to a uniform downward volume flux of material at rate V.

The variables are made dimensionless using the scalings

$$\tilde{\boldsymbol{u}} = \frac{\boldsymbol{u}}{V}, \quad \tilde{\boldsymbol{x}} = \frac{\boldsymbol{x}}{\kappa/V}, \quad \tilde{T} = \frac{T - T^P}{\Delta T}, \quad \tilde{p} = \frac{p}{\mu\kappa/\Pi_0}, \quad \tilde{t} = \frac{t}{V^2/\kappa},$$

where κ is the thermal diffusivity, μ is the dynamic viscosity and Π_0 is a reference permeability. These scaling closely follow those used by Schulze & Worster (1999), with the exception of the compositions, which we do not rescale. The non-dimensional groups that are formed as a result of these scalings are three Rayleigh numbers and a Darcy number:

$$Ra = \frac{\alpha g \Pi_0 \Delta T}{\nu V}, \quad Ra_A = \frac{\beta_A g \Pi_0}{\nu V}, \quad Ra_B = \frac{\beta_B g \Pi_0}{\nu V}, \quad Da = \frac{\Pi_0 V^2}{\kappa^2},$$

where g is the acceleration due to gravity and ν is the kinematic viscosity. In the dimensionless equations below, we drop the tildes.

The far-field boundary conditions in the liquid at $z = H$ are

$$T = T^H, \qquad A = A^H, \qquad B = B^H, \tag{2.6a}$$

$$\psi_z = \omega_z = 0. \tag{2.6b}$$

The last two boundary conditions enforce a parallel flow and a vorticity $\omega = -\nabla^2\psi$ that is not changing as it moves into or out of the domain. These conditions were adopted by Schulze & Worster (2001) in favour of conditions that force a uniform inflow, as the latter type of condition does not allow the possibility of a buoyant plume escaping the domain.

In the liquid layer, we assume that the fluid flow can be described by the Stokes equation. The additional equations in the liquid region include conservation of heat and solute, where we neglect solute diffusion. These equations have the form

$$Da\nabla^4\psi = Ra\frac{\partial T}{\partial x} + Ra_A\frac{\partial A}{\partial x} + Ra_B\frac{\partial B}{\partial x}, \tag{2.7a}$$

$$\left(\frac{\partial}{\partial t} - \frac{\partial}{\partial z}\right)T + \boldsymbol{u}\cdot\nabla T = \nabla^2 T, \tag{2.7b}$$

$$\left(\frac{\partial}{\partial t} - \frac{\partial}{\partial z}\right)A + \boldsymbol{u}\cdot\nabla A = 0, \tag{2.7c}$$

$$\left(\frac{\partial}{\partial t} - \frac{\partial}{\partial z}\right)B + \boldsymbol{u}\cdot\nabla B = 0. \tag{2.7d}$$

The two solute equations, (2.7c) and (2.7d), and boundary conditions, (2.6a), can be used to show $A = A^H$ and $B = B^H$ throughout the liquid layer. An important consequence of this is that there is no solutal buoyancy in the liquid unless a plume emerges from the mushy zone. The generalized tie-line constraint, discussed below, can also be traced to this fact. Later, we shall be focused principally on situations without thermal buoyancy, as this effect is normally dominated by solutal buoyancy during convection driven from a mushy zone.

The appropriate boundary conditions at liquid–mush interfaces have been discussed extensively by Schulze & Worster (1999, 2005). Briefly, continuity considerations lead to no jump in the temperature, pressure and normal velocity. With the flow into the mushy layer along a steadily solidifying interface, which is the only situation considered here, solid fraction characteristics emerge from the interface with $\phi = 0$ on the boundary. Continuity of solid fraction then gives rise to continuity of the temperature gradient – even if the effects of latent heat are included. An additional condition on the velocity is required on the liquid side of the interface, where (2.7a) is fourth order. Many authors use a no-slip condition with respect to the solid phase at liquid–porous media boundaries; others allow some form of slip based on a variety of arguments ranging from empirical observation to homogenization theory. We have chosen to enforce continuity of the tangential velocity in view of the fact that the solid-fraction vanishes at the interface. This also has the advantage that a novel condition on the vorticity can be derived from the resulting set of boundary conditions and used in place of the condition on the pressure. This condition is implemented in the linear stability analysis (equation (3.8d)) and in the fully nonlinear numerical solution (see equation (4.3)). Finally, the position of the free-boundary itself is determined by the liquidus constraint, extended to the liquid side of the interface. This expresses the

notion that the dendrites expand as far as possible in order to eliminate constitutional undercooling in the liquid (Worster 1986). Thus, owing to a combination of scaling and the uniform inlet concentration mentioned above, the interface is pinned to the $T=0$ isotherm. Taken together, these considerations lead to the following conditions applied at $z=h^P$:

$$[T]^+_- = [\hat{n}\cdot\nabla T]^+_- = [\boldsymbol{u}\cdot\hat{n}]^+_- = [\boldsymbol{u}\cdot\hat{t}]^+_- = [p]^+_- = \phi_A|^- = T|^+ = 0. \tag{2.8}$$

Turning to the primary mushy zone, we discuss some general consequences of the assumption of local equilibrium throughout the primary mushy layer before giving the full set of governing equations. In particular, we show that a tie-line constraint can be applied in this case. We follow the example of models used for binary alloys and assume that the compositions and temperature are constrained to the liquidus surface, $T=T^{\mathscr{L}}(A,B)$. Thus the temperature and composition do not evolve independently and the solid fraction must adjust to maintain conservation of species according to

$$\left(\frac{\partial}{\partial t}-\frac{\partial}{\partial z}\right)\mathscr{A}+\boldsymbol{u}\cdot\nabla A=0, \tag{2.9a}$$

$$\left(\frac{\partial}{\partial t}-\frac{\partial}{\partial z}\right)\mathscr{B}+\boldsymbol{u}\cdot\nabla B=0, \tag{2.9b}$$

where associated bulk compositions are defined as

$$\mathscr{A}=\chi A+\phi_A, \quad \mathscr{B}=\chi B+\phi_B. \tag{2.10}$$

Together, equations (2.9a) and (2.9b) imply a generalized tie-line constraint where the ratio of the compositions of passive species – B and C under our present conventions– remains fixed within the primary mushy layer along paths that move with the liquid velocity. To see why this must hold, it is easier to work with the compositions of the passive species. We may replace $\mathscr{B}$ with χB, and similarly for species C, but not for species A, as ϕ_A is non-zero in the primary mushy layer. These replacements yield an equation of the form

$$\chi\left(\frac{\partial}{\partial t}-\frac{\partial}{\partial z}\right)B+B\left(\frac{\partial}{\partial t}-\frac{\partial}{\partial z}\right)\chi+\boldsymbol{u}\cdot\nabla B=0,$$

and similarly for C. Eliminating $(\partial/\partial t-\partial/\partial z)\,\chi$ from these two equations leads to, after some manipulation, a single equation of the form

$$\left(\frac{\partial}{\partial t}-\frac{\partial}{\partial z}+\frac{\boldsymbol{u}}{\chi}\cdot\nabla\right)\frac{B}{C}=0. \tag{2.11}$$

The operator in this equation can be interpreted as a total derivative moving with an average liquid velocity $\boldsymbol{u}/\chi-\hat{\boldsymbol{k}}$ in the laboratory frame of reference, implying that the ratio of B and C is invariant moving with the liquid phase. Since their inlet compositions are in a fixed ratio across the top of the primary mushy layer, they remain that way within this layer. With both the liquidus constraint and tie-line constraint (2.11) enforced within the primary layer, all of the compositions are determined from the temperature field and solute conservation can be used as an evolution equation for the solid fraction. This is why there are no boundary conditions listed in (2.8) for the concentration fields. It is important to note that the tie-line constraint does not apply in cases where solute diffusion is present (Anderson 2003) and must be modified in situations where fluid enters a mushy zone along a boundary with varying concentration ratios. This type of situation would be encountered, for

example, after a primary mush inclusion has formed within the secondary mush owing to re-dissolution of the secondary species.

The governing equations in the primary mushy layer are then Darcy's equation, which we recast in terms of the streamfunction after taking its curl, conservation of heat and solute species A, the tie-line and liquidus constraints:

$$\nabla^2\psi = -Ra_P \Pi \frac{\partial T}{\partial x} + \frac{\nabla\Pi\cdot\nabla\psi}{\Pi}, \tag{2.12a}$$

$$\left(\frac{\partial}{\partial t} - \frac{\partial}{\partial z}\right)T + \boldsymbol{u}\cdot\nabla T = \nabla^2 T, \tag{2.12b}$$

$$\left(\frac{\partial}{\partial t} - \frac{\partial}{\partial z}\right)\mathscr{A} + \boldsymbol{u}\cdot\nabla A = 0, \tag{2.12c}$$

$$B = \frac{B^P}{1-A^P}(1-A), \tag{2.12d}$$

$$T = T^{\mathscr{L}}(A, B), \tag{2.12e}$$

where Π is the dimensionless permeability function whose form is specified in (2.18). Accompanying these equations is $\phi_B = 0$ so that $\phi_A + \chi = 1$ throughout the primary mushy layer. We emphasis that the relations (2.10) between bulk composition and solid fraction allow us to interpret (2.12*c*) as an equation for ϕ_A (or equivalently χ) and the tie-line and liquidus constraints (2.12*d*) and (2.12*e*) as equations for the compositions A and B. Another important consequence of the tie-line and liquidus constraints is that a single effective Rayleigh number appears in the momentum equation (2.12*a*) for the primary mushy layer:

$$Ra_P = Ra + \frac{Ra_A(1-A^P) - Ra_B B^P}{M_A(1-A^P) - M_B B^P}. \tag{2.13}$$

Following arguments similar to those presented above, the boundary conditions at the mush–mush interface $z = h^S$ are

$$[T]^+_- = [\hat{\boldsymbol{n}}\cdot\nabla T]^+_- = [p]^+_- = [\boldsymbol{u}\cdot\hat{\boldsymbol{n}}]^+_- = [\phi_A]^+_- = \phi_B|^- = 0, \tag{2.14a}$$

$$T = T^S|^+. \tag{2.14b}$$

Note that the temperature T^S can be deduced by identifying the intersection of the tie-line and the cotectic constraints on the phase diagram and extending the latter constraint to apply on the primary mushy-layer side of the interface. This generalizes the notion of marginal equilibrium by assuming that the secondary mushy-layer expands just enough to relieve any supercooling. Also, for the mush–mush interface in the present case, the condition of continuous pressure across the interface is equivalent to continuity of tangential velocity when the solid fraction (and hence permeabilities) and species concentrations are also continuous. This is seen by using Darcy's equation to transfer the continuity of the pressure (and hence pressure gradient) along the interface to the velocity field. In the work of McKibbin & O'Sullivan (1980), who addressed convection in layered porous media of different permeability values, the condition of pressure continuity does not reduce to continuity of tangential velocity.

The governing equations in the secondary mushy layer are the same as in the primary mushy layer with the exception that two cotectic constraints replace the liquidus and tie-line constraints and both solute balance equations are required to

evolve the two solid fractions ϕ_A and ϕ_B:

$$\nabla^2\psi = -Ra_S\Pi\frac{\partial T}{\partial x} + \frac{\nabla\Pi\cdot\nabla\psi}{\Pi}, \tag{2.15a}$$

$$\left(\frac{\partial}{\partial t} - \frac{\partial}{\partial z}\right)T + \boldsymbol{u}\cdot\nabla T = \nabla^2 T, \tag{2.15b}$$

$$\left(\frac{\partial}{\partial t} - \frac{\partial}{\partial z}\right)\mathscr{A} + \boldsymbol{u}\cdot\nabla A = 0, \tag{2.15c}$$

$$\left(\frac{\partial}{\partial t} - \frac{\partial}{\partial z}\right)\mathscr{B} + \boldsymbol{u}\cdot\nabla B = 0, \tag{2.15d}$$

$$A = A^{\mathscr{C}}(T), \tag{2.15e}$$

$$B = B^{\mathscr{C}}(T), \tag{2.15f}$$

where a second effective Rayleigh number can be identified

$$Ra_S = Ra + \frac{Ra_A}{M_A^{\mathscr{C}}} + \frac{Ra_B}{M_B^{\mathscr{C}}}. \tag{2.16}$$

The boundary conditions at the eutectic interface $z=0$ are simply

$$T = -1,\ \boldsymbol{u}\cdot\hat{\boldsymbol{n}} = 0. \tag{2.17}$$

Note that by definition of the cotectic lines, $A = A^E$ and $B = B^E$ automatically when $T=-1$. If the $z=0$ boundary were held at a temperature below the eutectic, the solid–mush interface would become an additional free- boundary requiring a full set of matching conditions.

Finally, in the work that follows we take the dimensionless permeability to be

$$\Pi(\chi) = \chi^3. \tag{2.18}$$

3. Linear stability analysis

We begin to examine the convective properties of the system in § 2 by way of a linear stability analysis. In § 3.1 we describe the base state solution, in § 3.2 we outline the linearized equations and in § 3.3 we describe the numerical method used to solve them.

3.1. *Base state*

The base state is a solution of the governing equations that is one dimensional, steady in the moving frame and has no buoyancy-driven flow ($\boldsymbol{u}=0$). We denote the base state with overbars. In the liquid layer $\bar{h}^P \leqslant z \leqslant H$,

$$\bar{T} = T^H - T^H\left(\frac{\mathrm{e}^{-z} - \mathrm{e}^{-H}}{\mathrm{e}^{-\bar{h}^P} - \mathrm{e}^{-H}}\right), \tag{3.1a}$$

$$\bar{A} = A^H, \quad \bar{B} = B^H. \tag{3.1b}$$

In the primary mushy layer $\bar{h}^S \leqslant z \leqslant \bar{h}^P$,

$$\bar{T} = T^S\left(\frac{\mathrm{e}^{-z} - \mathrm{e}^{-\bar{h}^P}}{\mathrm{e}^{-\bar{h}^S} - \mathrm{e}^{-\bar{h}^P}}\right), \tag{3.2a}$$

$$\bar{\chi} = \frac{M_A(A^H - 1) + M_B B^H}{M_A(A^E - 1) + M_B B^E + 1 + \bar{T}}, \tag{3.2b}$$

$$\bar{A} = \frac{A^H - 1}{\bar{\chi}} + 1, \tag{3.2c}$$

$$\bar{B} = \frac{B^H}{\bar{\chi}}, \tag{3.2d}$$

and $\bar{\phi}_A = 1 - \bar{\chi}$, $\bar{\phi}_B = \bar{\phi}_C = 0$, where the cotectic constraints can be used to show that

$$T^S = -1 + M_B^{\mathscr{C}}\left(\frac{B^H}{\chi^S} - B^E\right), \tag{3.3a}$$

$$\chi^S = \frac{M_A^{\mathscr{C}}(A^H - 1) - M_B^{\mathscr{C}} B^H}{M_A^{\mathscr{C}}(A^E - 1) - M_B^{\mathscr{C}} B^E}. \tag{3.3b}$$

In the secondary mushy layer $0 \leqslant z \leqslant \bar{h}^S$,

$$\bar{T} = T^S - (T^S + 1)\left(\frac{\mathrm{e}^{-z} - \mathrm{e}^{-\bar{h}^S}}{1 - \mathrm{e}^{-\bar{h}^S}}\right), \tag{3.4a}$$

$$\bar{A} = A^{\mathscr{C}}(\bar{T}), \tag{3.4b}$$

$$\bar{B} = B^{\mathscr{C}}(\bar{T}), \tag{3.4c}$$

$$\bar{\chi} = \frac{1 - A^H - B^H}{1 - \bar{A} - \bar{B}}, \tag{3.4d}$$

$$\bar{\phi}_A = A^H - \bar{A}\bar{\chi}, \tag{3.4e}$$

$$\bar{\phi}_B = 1 - \bar{\chi} - \bar{\phi}_A. \tag{3.4f}$$

Finally, upon applying the thermal gradient jump conditions at $z = \bar{h}^P$ and $z = \bar{h}^S$ we find that these interface positions are given by

$$\bar{h}^P = \ln\left(\frac{T^H + 1}{T^H + \mathrm{e}^{-H}}\right), \tag{3.5a}$$

$$\bar{h}^S = \ln\left(\frac{T^H + 1}{T^H - T^S + \mathrm{e}^{-H}(T^S + 1)}\right). \tag{3.5b}$$

3.2. *Linearized equations*

We examine the linear stability of this base-state solution by introducing infinitesimal perturbations and linearizing the system of governing equations with respect to these perturbations. Together, the base states and the perturbations in terms of normal modes take the form $T(x, z, t) = \bar{T}(z) + \hat{T}(z)\mathrm{e}^{\sigma t}\mathrm{e}^{i\alpha x}$, $\psi(x, z, t) = 0 + i\hat{\psi}(z)\mathrm{e}^{\sigma t}\mathrm{e}^{i\alpha x}$ and $h^P(x, t) = \bar{h}^P + \hat{h}^P\mathrm{e}^{\sigma t}\mathrm{e}^{i\alpha x}$.

The linearized system of equations is given below. In this case the composition perturbations can be decoupled from the remaining variables. In fact, in the liquid layer, $\hat{A} = \hat{B} = 0$. The far-field boundary conditions in the liquid at $z = H$ are

$$\hat{T} = \frac{\mathrm{d}\hat{\psi}}{\mathrm{d}z} = \frac{\mathrm{d}^3\hat{\psi}}{\mathrm{d}z^3} = 0. \tag{3.6}$$

The linearized equations in the liquid are

$$\frac{\mathrm{d}^4\hat{\psi}}{\mathrm{d}z^4} - 2\alpha^2\frac{\mathrm{d}\hat{\psi}}{\mathrm{d}z^2} + \alpha^4\hat{\psi} - \frac{\alpha Ra}{\mathrm{D}a}\hat{T} = 0, \tag{3.7a}$$

$$\frac{\mathrm{d}^2\hat{T}}{\mathrm{d}z^2} + \frac{\mathrm{d}\hat{T}}{\mathrm{d}z} - \alpha^2\hat{T} + \alpha\frac{\mathrm{d}\bar{T}}{\mathrm{d}z}\hat{\psi} = \sigma\hat{T}. \tag{3.7b}$$

The linearized boundary conditions for the perturbed quantities at $z=\bar{h}^P$ are

$$[\hat{T}]^+_- = \left[\frac{\mathrm{d}\hat{T}}{\mathrm{d}z}\right]^+_- = [\hat{\psi}]^+_- = \left[\frac{\mathrm{d}\hat{\psi}}{\mathrm{d}z}\right]^+_- = 0, \tag{3.8a}$$

$$\hat{T} + \hat{h}^P \frac{\mathrm{d}\bar{T}}{\mathrm{d}z} = 0, \tag{3.8b}$$

$$\left(\hat{\chi} + \hat{h}^P \frac{\mathrm{d}\bar{\chi}}{\mathrm{d}z}\right)\Big|^- = 0, \tag{3.8c}$$

$$\frac{\mathrm{d}\hat{\psi}}{\mathrm{d}z}\Big|^- - Da\left(\alpha^2 \frac{\mathrm{d}\hat{\psi}}{\mathrm{d}z} - \frac{\mathrm{d}^3\hat{\psi}}{\mathrm{d}z^3}\right)\Big|^+ = 0. \tag{3.8d}$$

The linearized equations in the primary mushy layer are

$$\frac{\mathrm{d}^2\hat{\psi}}{\mathrm{d}z^2} - \frac{1}{\Pi(\bar{\chi})}\frac{\mathrm{d}\Pi(\bar{\chi})}{\mathrm{d}\chi}\frac{\mathrm{d}\bar{\chi}}{\mathrm{d}z}\frac{\mathrm{d}\hat{\psi}}{\mathrm{d}z} - \alpha^2\hat{\psi} + \alpha Ra_P \Pi(\bar{\chi})\hat{T} = 0, \tag{3.9a}$$

$$\frac{\mathrm{d}^2\hat{T}}{\mathrm{d}z^2} + \frac{\mathrm{d}\hat{T}}{\mathrm{d}z} - \alpha^2\hat{T} + \alpha\frac{\mathrm{d}\bar{T}}{\mathrm{d}z}\hat{\psi} = \sigma\hat{T}, \tag{3.9b}$$

$$\frac{\mathrm{d}}{\mathrm{d}z}[\bar{\chi}\hat{T} + (\bar{T} - T^A)\hat{\chi}] + \alpha\frac{\mathrm{d}\bar{T}}{\mathrm{d}z}\hat{\psi} = \sigma[\bar{\chi}\hat{T} + (\bar{T} - T^A)\hat{\chi}], \tag{3.9c}$$

where $T^A = -1 + M_A(1 - A^E) - M_B B^E$.

The linearized boundary conditions for the perturbed quantities at $z=\bar{h}^S$ are

$$[\hat{T}]^+_- = \left[\frac{\mathrm{d}\hat{T}}{\mathrm{d}z}\right]^+_- = [\hat{\psi}]^+_- = \left[\frac{\mathrm{d}\hat{\psi}}{\mathrm{d}z}\right]^+_- = 0, \tag{3.10a}$$

$$\hat{T} + \hat{h}^S \frac{\mathrm{d}\bar{T}}{\mathrm{d}z} = 0, \tag{3.10b}$$

$$\left[\hat{\chi} + \hat{h}^S \frac{\mathrm{d}\bar{\chi}}{\mathrm{d}z}\right]^+_- = 0, \tag{3.10c}$$

$$\left(\hat{\phi}_A + \hat{h}^S \frac{\mathrm{d}\bar{\phi}_A}{\mathrm{d}z}\right)\Big|^- = 0. \tag{3.10d}$$

The linearized equations in the secondary mushy layer are

$$\frac{\mathrm{d}^2\hat{\psi}}{\mathrm{d}z^2} - \frac{1}{\Pi(\bar{\chi})}\frac{\mathrm{d}\Pi(\bar{\chi})}{\mathrm{d}\chi}\frac{\mathrm{d}\bar{\chi}}{\mathrm{d}z}\frac{\mathrm{d}\hat{\psi}}{\mathrm{d}z} - \alpha^2\hat{\psi} + \alpha Ra_S \Pi(\bar{\chi})\hat{T} = 0, \tag{3.11a}$$

$$\frac{\mathrm{d}^2\hat{T}}{\mathrm{d}z^2} + \frac{\mathrm{d}\hat{T}}{\mathrm{d}z} - \alpha^2\hat{T} + \alpha\frac{\mathrm{d}\bar{T}}{\mathrm{d}z}\hat{\psi} = \sigma\hat{T}, \tag{3.11b}$$

$$\frac{\mathrm{d}}{\mathrm{d}z}\left[\bar{\chi}\hat{T} + (\bar{T} - T^\star_A)\hat{\chi} + M^{\mathscr{C}}_A\hat{\phi}_A\right] + \alpha\frac{\mathrm{d}\bar{T}}{\mathrm{d}z}\hat{\psi} = \sigma\left[\bar{\chi}\hat{T} + (\bar{T} - T^\star_A)\hat{\chi} + M^{\mathscr{C}}_A\hat{\phi}_A\right], \tag{3.11c}$$

$$\frac{\mathrm{d}}{\mathrm{d}z}\left[\bar{\chi}\hat{T} + (\bar{T} - T^\star_B)\hat{\chi} - M^{\mathscr{C}}_B\hat{\phi}_A\right] + \alpha\frac{\mathrm{d}\bar{T}}{\mathrm{d}z}\hat{\psi} = \sigma\left[\bar{\chi}\hat{T} + (\bar{T} - T^\star_B)\hat{\chi} - M^{\mathscr{C}}_B\hat{\phi}_A\right], \tag{3.11d}$$

where $T^\star_A = -1 - M^{\mathscr{C}}_A A^E$ and $T^\star_B = -1 - M^{\mathscr{C}}_B(1 - B^E)$.

The linearized boundary conditions for the perturbed quantities at $z=0$ are

$$\hat{T} = \hat{\psi} = 0. \tag{3.12}$$

3.3. *Linearized equations: solution method*

We solve this linear system by implementing a pseudo-spectral Chebyshev method (Trefethen 2000). We outline some of the key steps below. First, we rescale each layer onto the interval $-1 \leqslant z' \leqslant 1$, where

$$z' = \frac{2(z-h^+)}{h^+ - h^-} + 1. \tag{3.13}$$

In the liquid layer $h^+ = H$ and $h^- = \bar{h}^P$, in the primary mushy layer $h^+ = \bar{h}^P$ and $h^- = \bar{h}^S$ and in the secondary mushy layer $h^+ = \bar{h}^S$ and $h^- = 0$. We discretize the vertical coordinate in each of the three layers (liquid, primary mush and secondary mush) using Chebyshev points

$$z'_j = \cos\left(\frac{j\pi}{N}\right), \quad j = 0, 1, 2, \ldots, N, \tag{3.14}$$

where $N = N_L$ in the liquid layer, $N = N_P$ in the primary layer and $N = N_S$ in the secondary layer. The dependent variables are also discretized. Derivatives are computed using Chebyshev differentiation matrices as described by the Matlab implementation cheb.m in Trefethen. This discretization leads to a generalized eigenvalue problem of the form $Ay = \sigma By$ where A and B are $(2N_L + 3N_P + 4N_S + 11) \times (2N_L + 3N_P + 4N_S + 11)$ matrices representing the system of linearized equations and boundary conditions, σ is the eigenvalue and y is a vector whose components are the discretized values of the dependent variables through the liquid layer, primary mushy layer and secondary mushy layer, including the unknowns $\hat{h}^P$ and $\hat{h}^S$. The calculations shown in this paper have $N_L = N_P = N_S = 16$.

We solve for the eigenvalues and eigenfunctions as functions of the system parameters; in particular, $\sigma = \sigma(\alpha, Ra, Ra_P, Ra_S, Da)$ where the dependence on the base state parameters and the phase diagram has been suppressed. As described in more detail in § 5, for a given set of parameters associated with the base state we examine the influence of the two Rayleigh numbers Ra_P and Ra_S and the wavenumber α on linear convection. In particular, for the case of neutral stability, we seek combinations of these two Rayleigh numbers as α varies, for which the largest $Re(\sigma)$ is zero. Oscillatory modes of instability were not observed for the parameters investigated.

4. Nonlinear convection

In this section, we describe the computational procedures used to find nonlinear steady solutions to the system of equations defined in § 2. We use a combination of Gauss–Seidel iteration and successive over-relaxation to iteratively update the various fields governed by elliptic equations until a steady solution is reached. On each iteration, this procedure is supplemented with a numerical integration to determine bulk compositions and a relaxation of the interface positions.

We impose symmetry conditions along the vertical boundaries at $x=0$ and $x=L$ for all three subdomains, so that we seek steady periodic solutions by solving for half of a convection cell. As L approaches the preferred wavelength, it is also possible to compute a full convection cell with the same equations.

Since we are neglecting the diffusion of solute, the compositions retain their far-field values throughout the liquid domain and there are no solute gradients to drive convection in the liquid region. For the nonlinear problem, we consider only the case $Ra = 0$, i.e. no thermal buoyancy. Working in a streamfunction–vorticity formulation, this leaves us with three elliptic equations in the liquid region:

$$\nabla^2 \psi = -\omega, \tag{4.1a}$$

$$\nabla^2 \omega = 0, \tag{4.1b}$$

$$\nabla^2 T + T_z = \boldsymbol{u} \cdot \nabla T. \tag{4.1c}$$

We enforce the boundary conditions detailed in § 2 by matching the temperature and streamfunction, along with their normal derivatives, at the free boundaries. The coupling between the domains is a non-overlapped domain decomposition. In principle, we can form any two distinct linear combinations of the Neumann and Dirichlet data at the upper and lower sides of the interface and alternately apply the data from one region to the boundary of the second. In the case of Laplace's equation, this is a stable algorithm except in the notable case of passing Dirichlet data in one direction and Neumann in the other. While the calculations of Schulze & Worster (1999) suggest this instability is suppressed by the translation term in (4.1c), we used the combinations

$$[T \pm \gamma_1 \hat{\boldsymbol{n}} \cdot \nabla T]_-^+ = 0, \qquad [\psi \pm \gamma_2 \hat{\boldsymbol{n}} \cdot \nabla \psi]_-^+ = 0, \tag{4.2}$$

to apply these boundary conditions. The constants γ_1 and γ_2 are arbitrary and were chosen to balance the magnitude of the Dirchlet and Neuman data. Using Darcy's equation, Stokes equation, the continuity of both velocity components and the pressure boundary condition at $z = h^P$, we arrive at

$$\hat{\boldsymbol{n}} \cdot \nabla \omega|^+ = \frac{1}{Da} \hat{\boldsymbol{n}} \cdot \nabla \psi|^-, \tag{4.3}$$

which we employ as a vorticity boundary condition by using data from the previous iteration to evaluate (i.e. backstep) the right-hand side of the equation. While this solves the problem of finding a vorticity boundary condition, it has the disadvantage of being singular in the limit of small Darcy number. The Darcy number is normally a very small parameter for porous media – of the order of 10^{-3} or smaller – so we went to some length to verify that our choice of $Da = 0.05$ was not compromising our results. Our investigation indicated this parameter has a relatively mild influence on stability over the range of Darcy number $Da \leqslant 0.05$. This is discussed further below, but for now we note that (4.3) is the only place where the Darcy number enters our model, owing to the absence of density gradients in the liquid region. This may seem surprising as one associates this parameter with permeability and, therefore, with the porous medium, but, in this model, the effects of permeability are largely represented through the Rayleigh numbers, which characterize the bulk properties of the porous media.

In the primary mushy layer, we iterate on the elliptic form of Darcy's equation (2.12*a*) and the stationary heat equation,

$$\nabla^2 T + T_z = \boldsymbol{u} \cdot \nabla T, \tag{4.4}$$

and directly integrate

$$\mathscr{A}_z = \boldsymbol{u} \cdot \nabla A, \tag{4.5}$$

for the bulk composition $\mathscr{A}$ by back-stepping the advective term. From this we can update the solid-fraction ϕ_A and permeability Π. Note that this integration must proceed downward from the top of the layer, where the boundary condition $\phi = \phi_A = 0$ applies.

At the mush–mush interface, we match the streamfunction, temperature and their derivatives in the manner described above. The secondary mush inherits the value of ϕ_A and the additional boundary condition $\phi_B = 0$. In this layer, we integrate to determine the bulk composition $\mathscr{B}$ as well as $\mathscr{A}$. The equations and procedures are the same as in the primary layer.

The computations are carried out on transformed versions of the equations that map the domain into three adjacent rectangular domains. The general form of this transformation is

$$\xi = \frac{x}{L}, \quad \zeta = \frac{z - h^-(x)}{h^+(x) - h^-(x)},$$

where L is the domain width, $h^+(x)$ is the upper boundary of the subdomain and $h^-(x)$ is the lower boundary. These transformations introduce a number of additional nonlinear terms, including terms explicitly involving the interface positions $z = h^P$ and $z = h^S$, into the bulk equations. The interface positions are updated on each iteration by relaxing them toward the isotherms $T = 0$ at $z = h^P$ and $T = T^S$ at $z = h^S$. All of the nonlinear computations shown in this paper have a 64×32 grid resolution on each of the three rectangular domains, which was more than sufficient to obtain good agreement with the linear calculations of § 2 where this comparison could be made. (We found that calculations with higher resolutions started to show higher numerical roundoff than truncation error in the limit where the amplitude of the buoyancy-driven flow vanished.)

Finally, as many of the computed nonlinear solutions lie along unstable subcritical bifurcations, we employ a continuation scheme that trades the specification of some linear combination of the two effective Rayleigh numbers Ra_P and Ra_S for the specification of the streamfunction value at a selected grid point (I, J). Note that only a single data point $\psi_{I,J}$ can be used because the linear combination of Rayleigh numbers is to replace that unknown in the system of equations being solved. Alternatively, we can use a norm of the solution, but this is far more expensive. Either way, we essentially fix the amplitude of the solution and iterate to obtain the correct Rayleigh numbers rather than fixing the Rayleigh numbers and letting the iteration scheme evolve naturally, in which case we would miss unstable steady states. An efficient way of implementing this scheme is to write down the discretized model and solve for the Rayleigh number. This explicit formula can then be used to update the streamfunction at the coordinates (I, J). For this, it is best to start the sweep through the grid at (I, J), so that the value obtained is consistent with the Rayleigh number predicted by the explicit difference formula.

5. Results

All of the results discussed in this section correspond to a material with a symmetric phase diagram (see figure 1 and table 1), zero thermal Rayleigh number $Ra = 0$, far-field temperature $T^H = 0.4$, Darcy number $Da = 0.05$ (unless otherwise noted) and a domain height $H = 2$.

The parameters that control the characteristics of the base-state solution include the far-field temperature and the initial liquid composition (i.e. far-field compositions in the liquid layer). The total depth of the combined mushy layers is controlled by the

	I	II	III
A^H	0.37	0.55	0.46
B^H	0.35	0.35	0.44
C^H	0.28	0.10	0.10
T^H	0.4	0.4	0.4
A^S	0.357143	0.4375	0.448980
B^S	0.357143	0.4375	0.448980
C^S	0.285714	0.125	0.10204
T^S	−0.350649	−0.519231	−0.087003
h^P	0.961	0.961	0.961
h^S	0.513	0.352	0.830
$\phi(z=h^S)$	0.02	0.2	0.02
$\phi(z=0)$	0.16	0.7	0.7

TABLE 1. Parameter values that characterize the solidification path on the phase diagram for base state configurations I, II and III and also key parameters calculated from the base-state solution. In all cases considered here $A^E = B^E = C^E = 1/3$, $A^P = A^H$, $B^P = B^H$ and $C^P = C^H$. Additionally, by our choice of non-dimensionalization, $T^P = 0$ and $T^E = -1$. The parameter values at point S are not independent – they can be computed from the constraints placed on the phase diagram.

far-field temperature T^H which we have fixed for simplicity. Additionally, the base-state solid fraction is an increasing function of depth into the mushy layers, which implies that the permeability is a decreasing function of depth. Consequently, the secondary mushy layer is less permeable than the primary mushy layer. The initial compositions are key controls of the base-state properties such as the relative thicknesses of the primary and secondary mushy layers and the permeabilities (or solid fractions) of each layer. We have extensively explored different initial compositions throughout the ternary phase diagram and have identified the following general trends. First, if we fix the value of B and reduce the value of C (corresponding to approaching the A–B side of the ternary phase diagram) the secondary-layer thickness increases at the expense of the primary-layer thickness and the solid fractions in both primary and secondary layers increase. Secondly, if we fix C and increase B (approaching the A–B cotectic boundary), the secondary-layer thickness again increases at the expense of the primary-layer thickness. In this case, while the maximum solid fraction (at the bottom of the secondary mushy layer) remains constant, the maximum solid fraction in the primary layer goes down. These basic trends are consistent with those shown in figures 6 and 7 of Anderson (2003).

We emphasize that the various phase-diagram parameters determine the base state and, thus, influence convection primarily through the resulting solid-fraction profiles and mushy-layer thicknesses. With this observation in mind, we have organized our calculations with an eye toward understanding the influence of changes in the qualitative characteristics of the base states rather than by an extensive exploration of phase diagram parameters. In particular, we focus attention on three base-state configurations (denoted by I, II and III as in table 1), which are representative of the range of characteristics exhibited by the base state. Base state I has comparable mushy-layer thicknesses with relatively high permeabilities. Base state II has a relatively thin secondary mushy layer of low permeability. Base state III has a relatively thin primary mushy layer with high permeability and a thick secondary mushy layer with low permeability.

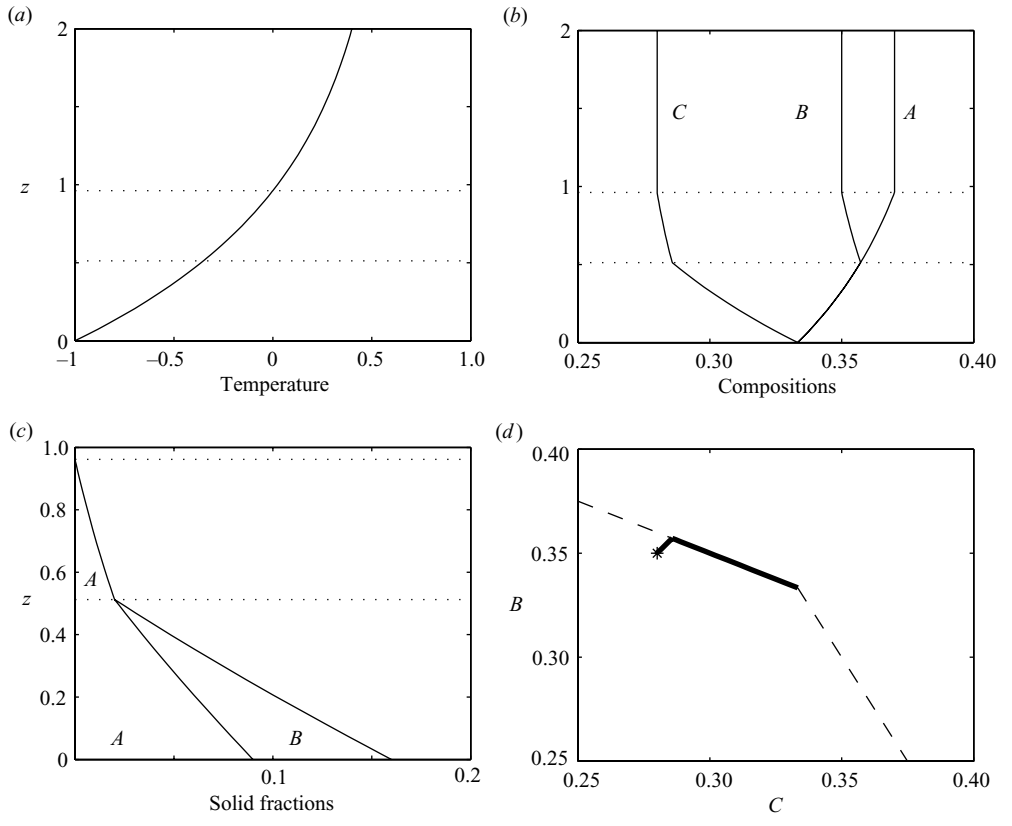

FIGURE 2. A plot of the base-state temperature, composition and solid-fraction profiles for the parameter values in table 1, base state I, along with a diagram indicating the solidification path on the ternary phase diagram.

While the above base-state properties influence the details of the flow, the parameters that control the characteristics of the convection are the two Rayleigh numbers and the wavenumber α (or domain width $L = \pi/\alpha$), all of which can be specified independently of the phase diagram parameters. As documented by Aitta *et al.* (2001*b*) and by Anderson (2003), for a given density function – which depends generally on temperature and composition – it is possible to identify solidification paths starting at different locations throughout the entire ternary phase diagram (i.e. making use of all three liquidus surfaces) that allow all possible combinations of stable and unstable density stratification through the two mushy layers to occur. In our model, changes in the base state characteristics (composition profiles, solid fraction profiles, etc.) that result from moving the initial composition from a point on one liquidus surface to its image on another can be addressed simply by an appropriate relabelling of the compositions A, B and C (in fact, we need only consider half of a single liquidus surface). Thus, the different density stratification scenarios realized by traversing the entire ternary phase diagram (for a given material system), may be addressed simply by treating Ra_P and Ra_S – the quantities that measure the density stratification – as parameters whose values (positive, negative or zero) may be independently specified for each base-state configuration under consideration here.

In order to make clear the general nature of the non-convecting state, we show in figure 2 the key properties of base-state I. Note that the base-state solution is

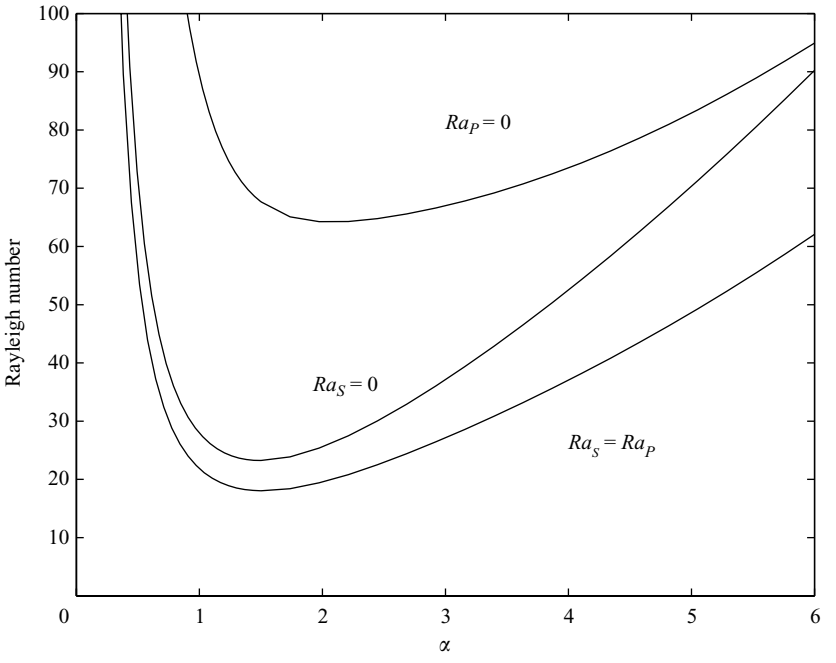

FIGURE 3. This figure shows neutral stability curves for base state I. The neutral curve for convection with equal Rayleigh numbers ($Ra_S = Ra_P$) has critical Rayleigh numbers $Ra_P = Ra_S = 18.04$ and wavenumber $\alpha = 1.52$. The neutral curve for convection driven from the primary mushy layer ($Ra_S = 0$) has critical Rayleigh number $Ra_P = 23.24$ and wavenumber $\alpha = 1.50$. The neutral curve for convection driven from the secondary mushy layer ($Ra_P = 0$) has critical Rayleigh number $Ra_S = 64.19$ and wavenumber $\alpha = 2.08$.

independent of all Rayleigh numbers and the wavelength. Figure 2(*a*) shows that the temperature is continuous and differentiable throughout the entire domain, owing to our simplifying assumptions of zero latent heat and equal thermal properties for all three components in both the liquid and solid phases. The dotted lines indicate the interface positions. The composition profiles, shown in figure 2(*b*) are constant in the liquid and have an exponential form in the mushy layers with discontinuous derivatives at the interfaces. The fact that $A = B$ at the secondary interface and $A = B = C$ at the eutectic front are the result of the symmetry of the system we have chosen to examine. Note that the composition values sum to unity along any horizontal line. The solid fraction profiles are shown in figure 2(*c*). The solid portion of the primary mushy layer consists only of material A, while the secondary mushy layer has solid material of type A and B. The curves in the secondary layer show the fraction of the solid that is material A and the total solid fraction. Thus, the fraction of material B is accounted for by the region between the curves, marked with the letter B. Finally, figure 2(*d*) indicates the path that the state of a representative control volume follows on the phase diagram as we move from the inlet conditions, marked with the star, down to the eutectic front. This path reflects the tie-line, liquidus and cotectic constraints. As indicated in table 1, base states II and III use different initial compositions and therefore differ from base state I primarily with respect to the maximum solid fraction and the thickness associated with each mushy layer.

The neutral stability curves shown in figure 3 correspond to base state I for the three cases of convection driven equally from both layers ($Ra_P = Ra_S$), from the primary

layer only (with $Ra_S = 0$) and from the secondary layer only (with $Ra_P = 0$). All three neutral stability curves exhibit a single-mode (i.e. local minimum) structure. In fact, all other cases investigated (including II and III, but also many other base, state configurations corresponding to different initial compositions in the ternary phase diagram) displayed only unimodal neutral curves. The unimodal characteristic of the neutral stability curve has been observed for the binary alloy mushy-layer system calculated by Worster (1992) for the case of zero solute diffusivity and, owing to our assumption of negligible solute diffusivity, is consistent with our observations.

The minimum Rayleigh number(s) and linear critical wavenumber can vary broadly. We have compiled this information in table 2 along with results from our nonlinear study, in which we were able to, in some cases, obtain independent estimates for the linear critical Rayleigh numbers. (The nonlinear data is missing in cases where the critical Rayleigh numbers were especially large or one of the layers was especially thin as, these conditions lead to numerical difficulties.) Following Beckermann *et al.* (2000), we introduce at this point two rescaled Rayleigh numbers that characterize more naturally the properties of each particular layer. In particular, each new Rayleigh number has the form $Ra^{nat} = (\Delta\rho/\rho_0) g \widetilde{\Pi} h/(\kappa\nu)$ so that each is based on the density difference $\Delta\rho$, thickness h and effective permeability $\widetilde{\Pi}$ for each layer (rather than reference values of these quantities that are less representative of each particular mushy layer). After some manipulations, these new Rayleigh numbers can be related to those defined above by

$$Ra_P^{nat} = Ra_P[-T^S(h^P - h^S)\widetilde{\Pi}_P], \tag{5.1}$$

$$Ra_S^{nat} = Ra_S[(T^S + 1)h^S\widetilde{\Pi}_S], \tag{5.2}$$

where $\tilde{\Pi}_P$ and $\tilde{\Pi}_S$ are dimensionless effective permeability values for each layer. For simplicity, we have defined $\tilde{\Pi}_P$ and $\tilde{\Pi}_S$ as $\tilde{\chi}_P^3$ and $\tilde{\chi}_S^3$; that is the cube of the average liquid fraction in each layer. The values of these rescaled Rayleigh numbers at the linear critical point are less variable from case to case compared to the original versions and thus provide a more unifying basis for predicting the onset of convection.

Table 2 is organized as follows. For each base state (I, II, III) we show five convective scenarios: (i) $Ra_S < 0$, $Ra_P > 0$ – a very stably stratified secondary layer with an unstably stratified primary layer; (ii) $Ra_S = 0$, $Ra_P > 0$ – a neutrally stratified secondary layer with an unstably stratified primary layer; (iii) $Ra_S = Ra_P$ – two unstably stratified mushy layers; (iv) $Ra_S > 0$, $Ra_P = 0$ – an unstably stratified secondary layer with a neutrally stratified primary layer; and (v) $Ra_S > 0$, $Ra_P < 0$ – an unstably stratified secondary layer with a very stably stratified primary layer. For each case, we have given the linear critical Rayleigh numbers and wavenumber calculated from the linear stability analysis and, where possible, the corresponding linear critical Rayleigh numbers calculated using the nonlinear code. Table 2 also gives further details about the bifurcating solutions, which we discuss in more detail below.

We point out the following general features of the results in table 2. First, the linear critical Rayleigh number varies broadly for the different base states and convective scenarios considered. The critical wavenumber tends to be larger for cases in which an unstable layer is paired with a stable layer; this is generally accompanied by a localization of the convection within the unstable layer. The largest wavenumbers were always observed in connection with convection isolated in the secondary mushy layer. In the case in which an opposing density stratification is not present, the convection tends to be of larger scale.

	Linear					Nonlinear			Inclusion			
	Ra_P	Ra_S	Ra_P^{nat}	Ra_S^{nat}	α_c	Ra_P	Ra_S	Bifurcation	Ra_P	Ra_S	Amplitude	Location
I	37.0	−60.0	5.64	−15.06	1.56	37.3	−60.5	Super.	37.4	−60.6	0.454	P
	23.24	0	3.54	0	1.50	23.3	0	Super.	23.6	0	0.512	P
	18.04	18.04	2.75	4.53	1.52	18.1	18.1	Super.	18.2	18.2	0.512	P
	0	64.19	0	16.11	2.08	0	64.6	Sub.	0	62.7	0.189	S
	−104.94	104.94	−15.99	26.34	4.48	−104	104	Sub.	−103.9	103.9	0.995	S
II	38.46	−150	8.87	−4.22	1.73	38.4	−150	Super.	39.1	−152.5	0.315	P
	35.31	0	8.14	0	1.73	35.5	0	Super.	35.8	0	0.308	P
	34.53	34.53	7.96	0.97	1.73	34.8	34.8	Super.	35.1	35.1	0.299	P
	0	730.25	0	20.59	4.43	–	–	–	–	–	–	–
	−1396	1396	−321.8	39.37	7.60	–	–	–	–	–	–	–
III	444.2	−444.2	4.93	−88.22	2.95	–	–	–	–	–	–	–
	151.9	0	1.69	0	1.93	–	–	–	–	–	–	–
	68.4	68.4	0.76	13.58	1.92	–	–	–	–	–	–	–
	0	115.0	0	22.84	2.01	–	–	–	–	–	–	–
	−1086.3	300	−12.06	59.58	3.77	–	–	–	–	–	–	–

TABLE 2. Results of linear and nonlinear calculations associated with five convection scenarios for the three different base state configurations I, II and III identified in table 1. In particular, the linear critical Rayleigh numbers (for two different sets of scalings) and the critical wavenumber are shown in the five columns under the linear heading. Under the nonlinear heading, where possible, we show the two Rayleigh numbers at zero amplitude to be compared with the corresponding ones from the linear analysis. We also indicate whether the bifurcation is supercritical (super.) or subcritical (sub.). Additionally, under the 'Inclusion' heading, we give the Rayleigh number values and amplitude (measured by the L_2 norm of the buoyancy-driven streamfunction) at which an inclusion forms. The final column indicates whether the inclusion forms as a liquid inclusion in the primary layer (P) or as a primary mushy layer inclusion in the secondary layer (S). For the calculation of the different Rayleigh numbers under the linear heading we note that $Ra_P = g_P Ra_P^{nat}$ and $Ra_S = g_S Ra_S^{nat}$ (base case I: $g_P = 0.1524$, $g_S = 0.2510$; base case II: $g_P = 0.2305$, $g_S = 0.0282$; base case III: $g_P = 0.0111$, $g_S = 0.1986$). For simplicity, we have defined $\widetilde{\Pi}_P$ and $\widetilde{\Pi}_S$ as $\widetilde{\chi}_P^3$ and $\widetilde{\chi}_S^3$; that is the cube of the average liquid fraction in each layer.

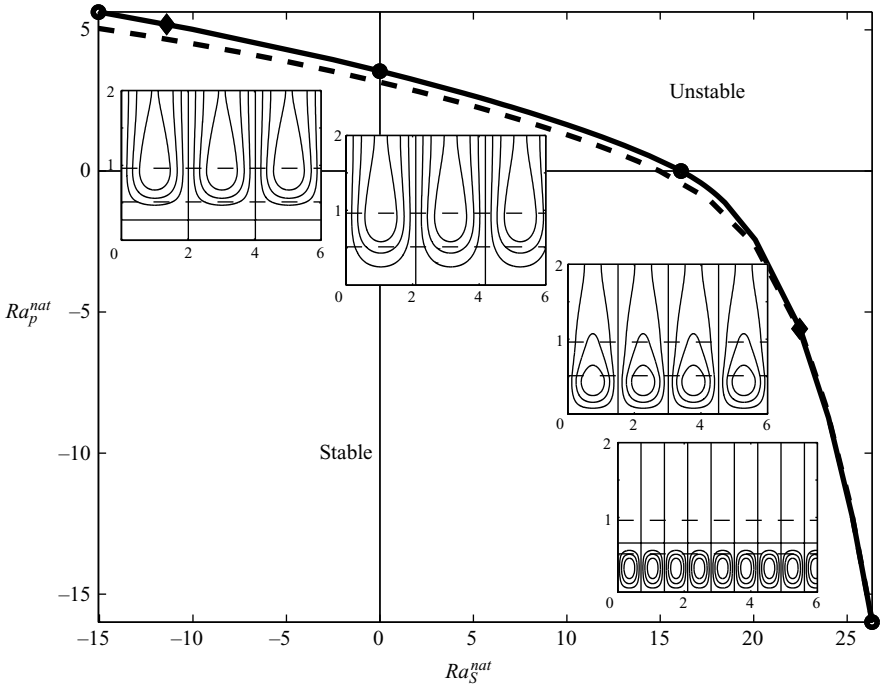

FIGURE 4. The main solid curve corresponds to the linear critical value of the Rayleigh numbers separating stable and unstable solutions for base case I using $Da = 0.05$. The dashed curve is the same result but with $Da = 10^{-5}$. Insets show the convection pattern at the four open circles along the main solid curve – moving from upper left to lower right. The leftmost diamond shows the approximate location of the transition point from one roll (on the right-hand side) to two stacked rolls (on the left-hand side). The rightmost diamond shows the approximate location of the transition from one roll (on the left-hand side) to two stacked rolls (on the right-hand side).

These trends can be observed in figures 4–6, where we map out in the (Ra_S^{nat}, Ra_P^{nat})-plane, an overall boundary between linearly stable and unstable regions. Figure 4 shows such results for base case I using the results of the linear stability analysis described in § 3. The solid curve in the main plot corresponds to the linear critical value of the Rayleigh numbers separating stable and unstable solutions using $Da = 0.05$. The four inset plots show the convective streamlines at parameter values indicated by the four open circles along the main solid curve – moving from upper left to lower right – and correspond to four of the five flow configurations detailed in table 2 (the convective pattern for the case with $Ra_P = Ra_S$ is very similar to the case $Ra_P > 0$, $Ra_S = 0$ and so is not shown here). In these insets, the horizontal dashed lines show interface positions separating the liquid layer, primary mushy layer and secondary mushy layer. In the upper left inset plot, where the secondary layer is very stably stratified, we see that the main convective flow occurs in the primary mushy layer and liquid layer. The solid horizontal line appearing in the secondary mushy layer is a separating streamline below which there is a very weak reverse flow. Comparing the four inset plots from left to right shows the convective flow eventually becoming localized in the secondary mushy layer. In the lower right inset, a small-scale convection pattern appears in the secondary layer. In this case, there is a weak reverse flow occurring in the primary layer (above the horizontal separating

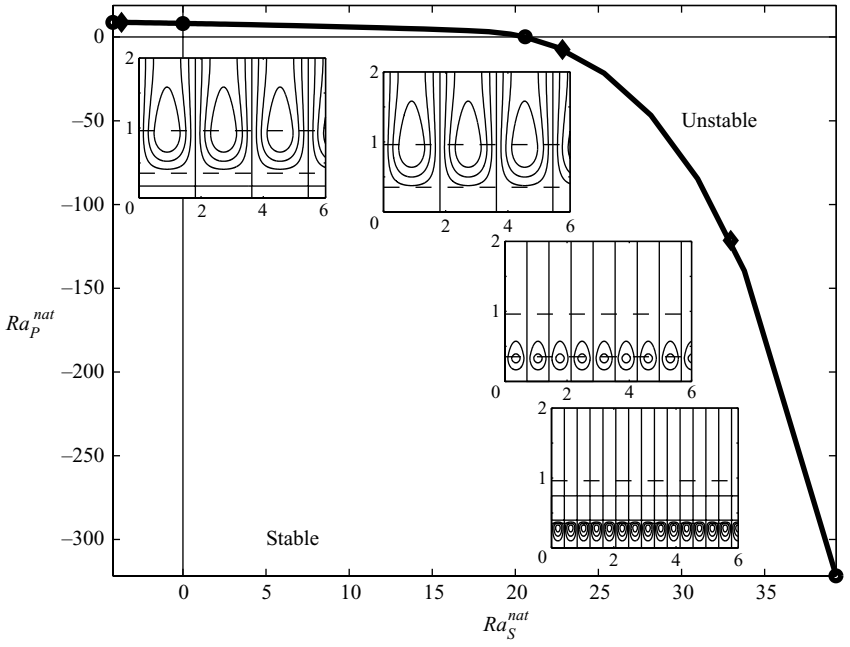

FIGURE 5. The main solid curve corresponds to the linear critical value of the Rayleigh numbers separating stable and unstable solutions for base case II using $Da = 0.05$. Inset plots show the buoyant convection at the four open circles – moving from upper left to lower right – indicated on the main plot. The leftmost diamond shows the approximate location of the transition point from one roll (on the right-hand side) to two stacked rolls (on the left-hand side). The middle diamond shows the approximate location of the transition from one roll (on the left-hand side) to two stacked rolls (on the right-hand side). The rightmost diamond shows the approximate location of the transition from two stacked rolls (on the left-hand side) to three stacked rolls (on the right-hand side).

streamline). We discuss these reverse flows and their impact on the solid fraction distribution in the mushy layers in the context of the nonlinear solutions below. The two open diamonds shown on the main solid curve indicate the points along the curve where the convective flow pattern makes a transition from single-cell flows to these stacked-cell flows. In particular, the leftmost diamond shows the approximate location of the transition point from one roll (on the right-hand side) to two stacked rolls (on the left-hand side). The rightmost diamond shows the approximate location of the transition from one roll (on the left) to two stacked rolls (on the right). Physically, the stacked cell case suggests that the main flow avoids the stably stratified region (whether it be in the primary or secondary mushy layer) where the resistance to convective flow is large and instead prefers a configuration in which a weak reverse flow is generated in the stably stratified region.

In figure 4, the dashed curve in the main plot shows the same result as the main solid curve, but with a much smaller value of the Darcy number $Da = 10^{-5}$ that is more representative of physical systems than $Da = 0.05$. We observe a destabilization of the flow (smaller Rayleigh numbers) primarily for the flow configurations in which there is significant flow in the primary mushy layer and liquid layer. Since the Darcy number enters our calculations only in the interfacial condition at the liquid–primary mush interface, the effect of changing Da becomes negligible for convection modes localized in the secondary mushy layer. Corresponding to the upper left-hand portion

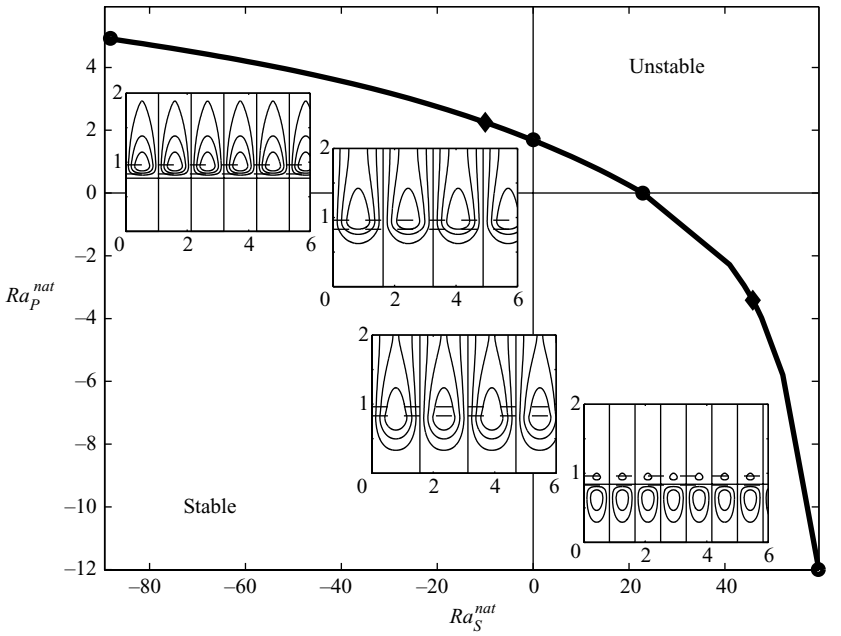

FIGURE 6. The main solid curve corresponds to the linear critical value of the Rayleigh numbers separating stable and unstable solutions for base case III using $Da = 0.05$. Inset plots show the buoyant convection at the four open circles – moving from upper left to lower right – indicated on the main plot. The leftmost diamond shows the approximate location of the transition point from one roll (on the right-hand side) to two stacked rolls (on the left-hand side). The rightmost diamond shows the approximate location of the transition from one roll (on the left-hand side) to two stacked rolls (on the right-hand side).

of the main plot where the difference between the solid and dashed curves can be observed, we note that the critical wavenumbers for the case $Da = 10^{-5}$ (dashed curve) are slightly larger (leading to a horizontally more compact set of rolls) than that for the case $Da = 0.05$ (solid curve). The overall effect of decreasing the Darcy number is to destabilize the system, consistent with observations in binary mushy-layer systems (Worster, 1992). As discussed in § 4, our choice of a somewhat large Darcy number is influenced by our implementation of (4.3) in the numerical solution of the governing equations. Note that the limit $Da \to 0$ implies a no-slip condition on the mush–liquid interface (Schulze & Worster 1998).

Figure 5 shows results analogous to those of figure 4 for base case II. Here the base state is less permeable overall, with a much thinner secondary layer. The main solid curve corresponds to $Da = 0.05$. The insets – from upper left to lower right – correspond to the four open circles indicated along the main solid curve. Again, in the two extreme cases, we observe stacked convection cells with weak reverse flow in the stably stratified layer. In fact, in the lower right-hand inset there are three stacked cells, although the cells driven in the primary mushy layer and liquid layer from the convection in the secondary layer are very weak. Along the main solid curve three open diamonds are indicated. The leftmost diamond shows the approximate location of the transition point from one roll (on the right) to two stacked rolls (on the left). The middle diamond shows the approximate location of the transition from one roll (on the left) to two stacked rolls (on the right). The rightmost diamond shows the approximate location of the transition from two stacked rolls (on the left) to three

stacked rolls (on the right). Finally, we again note the general trend of increasing wavenumber (decreasing wavelength) for the convection driven from the secondary layer.

Figure 6 shows results analogous to those of figure 4 for base case III. Here, the base state has a much thicker secondary layer (with much lower permeability) and a much thinner primary mushy layer compared to base case I. The main solid curve corresponds to $Da = 0.05$. The insets – from upper left to lower right – correspond to the four open circles indicated along the main solid curve. In the upper left-hand inset, the convection is driven from a very thin primary mushy layer. The main flow is confined to the primary and liquid layers, while a very weak reverse flow occurs in the relatively impermeable secondary layer. In the lower right-hand inset, the reverse flow, driven from the secondary layer, is centred around the primary mushy layer–liquid layer interface. On the main solid curve, the leftmost diamond shows the approximate location of the transition point from one roll (on the right) to two stacked rolls (on the left) and the rightmost diamond shows the approximate location of the transition from one roll (on the left) to two stacked rolls (on the right).

Before discussing the nonlinear results we comment on the validation of both the linear and nonlinear codes used in this paper. First, the base-state solutions given explicitly in § 3,.1 have been reproduced to a very high degree of accuracy using the nonlinear numerical methods described in § 4. Secondly, the neutral stability curves calculated as described in § 3 were consistently reproduced to within a few per cent using nonlinear solutions which maintained a fixed small amplitude while varying the domain width (see linear critical Rayleigh numbers given in table 2). The difference was attributable to the truncation error in the nonlinear code owing to a relatively coarse grid. Thirdly, both the linear and nonlinear codes used here have been validated by comparison with the previously computed binary results of Worster (1992) and Schulze & Worster (1999).

The computation of nonlinear finite-amplitude convecting solutions allows us to probe further into the interaction between the convective motion set up initially by the density stratification and the evolution (dissolution and/or growth) of the solid fraction in each layer. As a representative case, we shall show the nonlinear counterparts of the four convective scenarios highlighted for base case I in the insets of figure 4. For these nonlinear computations we fix the domain width in each case to a value that corresponds to the linear critical wavenumber (that is, $L = \pi/\alpha_c$). The amplitude of the flow is then increased in each case until the solid fraction (either ϕ_A in the primary layer or ϕ_B in the secondary layer) is driven to zero at some point along the centre of the cell where the downward flow is the weakest and the buoyancy-driven portion of the flow is directly upward. We find that such inclusions can occur either in the primary layer (in which case a liquid inclusion is formed) or in the secondary layer (in which case we observe a primary mushy-layer inclusion). This information is also included in table 2, the last five columns of which indicate the type of bifurcation, the values of the Rayleigh numbers and flow amplitude (norm of the buoyancy-driven streamfunction) and the location of the inclusion when it first forms upon increasing the amplitude.

Figure 7 shows the nonlinear flow for base case I(i) in which the secondary mushy layer is very stably stratified and the primary mushy layer is unstably stratified. In both plots, the two dark solid lines indicate the position of the interfaces separating the liquid layer, the primary mushy layer and the secondary mushy layer. These interface positions are notably perturbed from the linear stability case in which they are planar. In Figure 7(*a*) we show isotherms (dashed curves) and the buoyancy-driven

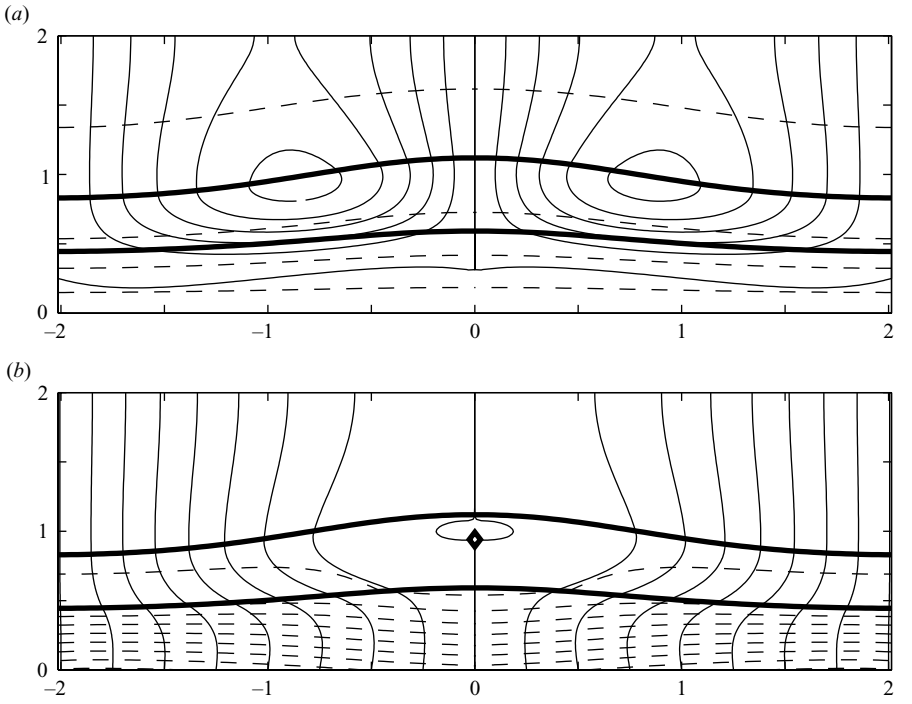

FIGURE 7. Nonlinear solutions for base case I(i). (*a*) Streamlines associated with the buoyant convection (solid curves using equal spacing of 0.1 between contours) and isotherms (dashed curves using equal spacing of 0.25 between contours). (*b*) Streamlines for the total mass flux (solid curves) and the total solid fraction (dashed curves using equal spacing of 0.02 between contours). The diamond shows the location of a liquid inclusion in the primary mushy layer.

streamlines (solid curves). Consistent with the upper left-hand inset plot in figure 4, we see that there is a separating streamline in the secondary layer below which a reverse flow occurs. Since this flow is very weak, these weak secondary rolls do not appear in the plot (for clarity in the main convective rolls, we have chosen equally spaced streamline values). In figure 7(*b*), we show the total solid fraction contours (dashed curves) and streamlines for the total mass flux, which has the streamfunction $\psi + x$ (solid curves entering at the top of the plot and exiting at the bottom). In the case of no buoyant convection, these streamlines would be undeflected vertical lines. Along the centreline in the primary mushy layer is shown a region of reverse circulation and, as indicated by the diamond, the location of a liquid inclusion in the primary mushy layer. As pointed out by Schulze & Worster (1999), such a liquid inclusion must occur at the bottom of the reverse circulation streamline. This observation provides another useful diagnostic for the nonlinear code. We note that the nonlinear calculations are not designed to compute the physically valid solution beyond the amplitude at which the inclusion forms and so we have taken care to capture the solution as close to the initial formation of the inclusion as possible.

Results for the other three nonlinear cases are shown in figures 8–10. In the sequence of figures for the nonlinear case, we have used the same isotherm contours, the same streamline values and the same solid fraction contours so that a more quantitative comparison can be made between the results. In particular, we can see that the convective flow becomes progressively weaker as the flow makes a transition

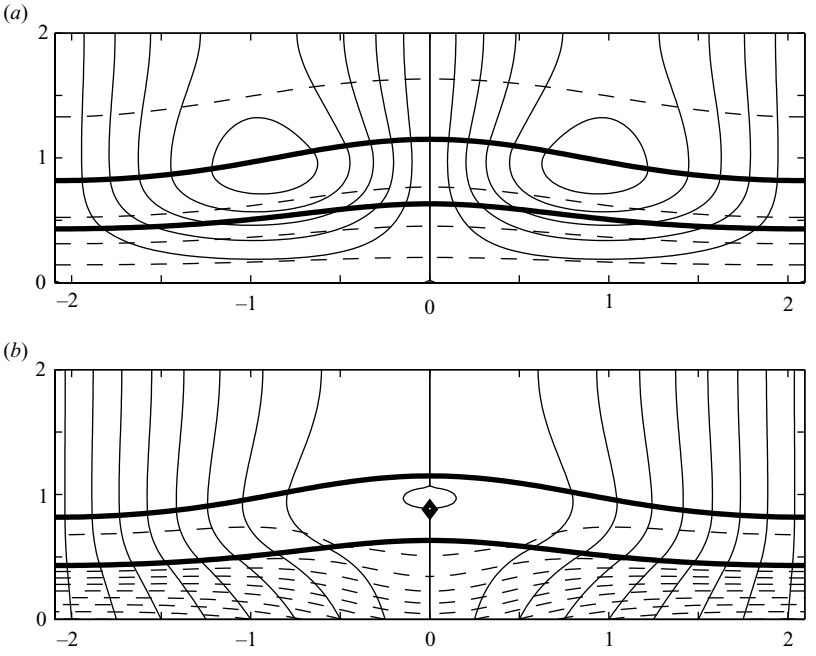

FIGURE 8. Nonlinear solutions for base case I(ii). (*a*) Streamlines associated with the buoyant convection (solid curves using equal spacing of 0.1 between contours) and isotherms (dashed curves using equal spacing of 0.25 between contours). (*b*) Streamlines for the total mass flux (solid curves) and the total solid fraction (dashed curves using equal spacing of 0.02 between contours). The diamond shows the location of a liquid inclusion in the primary mushy layer.

from being driven in the primary layer to being driven in the secondary layer. A comparison between figures 7 and 8 shows that the two cases are very similar, with the exception that the case with a very stably stratified secondary mushy layer has a weak reverse flow in the secondary mushy layer (figure 7) rather than a relatively deep penetration of the main flow into the secondary layer (figure 8). In both of these cases, a liquid inclusion forms in the primary mushy layer along the centreline. For the two flows driven from the secondary mushy layer, as shown in figures 9 and 10, we observe the formation of a primary mushy layer inclusion in the secondary mushy layer. For the case of a very stably stratified primary mushy layer, we note that there is again a weak reverse flow in the primary mushy layer corresponding to a stacked convective roll (figure 10). While the solid fraction contours in this case are depressed along the centreline in the secondary mushy layer (indicative of chimney formation where there is a strong upflow) they are very slightly elevated along the centreline in the primary mushy layer (where there is a downflow due to the reversed convection cells). Finally, we note that the deflection of the interface positions from horizontal becomes less pronounced for the cases in which the flow is driven from the secondary mushy layer. This is due to the overall relatively weak flow that occurs in these cases.

6. Conclusion

In this paper, we have adopted the model of ternary alloy solidification first analysed by Anderson (2003) in the context of diffusion-controlled growth from a fixed boundary and have applied it to study convective effects during directional

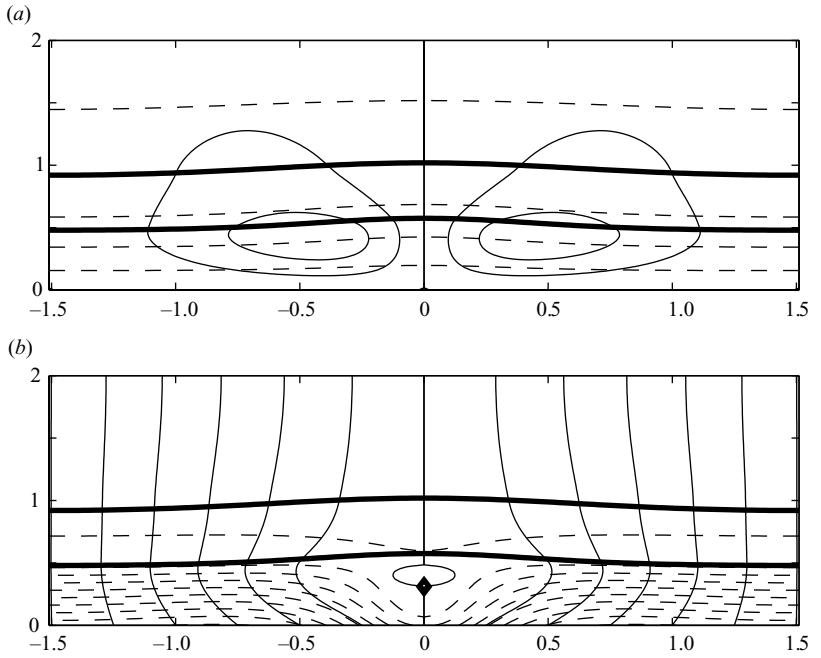

FIGURE 9. Nonlinear solutions for base case I(iv). (*a*) Streamlines associated with the buoyant convection (solid curves using equal spacing of 0.1 between contours) and isotherms (dashed curves using equal spacing of 0.25 between contours). (*b*) Streamlines for the total mass flux (solid curves) and the total solid fraction (dashed curves using equal spacing of 0.02 between contours). The diamond shows the location of a primary mush inclusion in the secondary mushy layer.

solidification at a steady rate V. We have performed a linear stability analysis of this system and have computed strongly nonlinear convective steady states that develop from the initial bifurcation. To this end, we have reduced the parameter set by a combination of scaling and simplifying assumptions to focus exclusively on the role of convection.

Before discussing our results in more detail, we emphasize two general conclusions concerning convection in ternary mushy zones. First, we found that the role of convection could be characterized by two Rayleigh numbers – one for each mushy layer – that combine all of the effects on the local density induced by changes in species compositions and the thermal environment. This generalizes the binary case (see Worster 1997) where the mushy layer can be characterized by a single Rayleigh number. Secondly, we found that, the tie-line constraint, (2.11), can be generalized to situations with fluid flow. As noted earlier, this condition is a consequence of negligible solutal diffusivity and the uniform inlet concentrations that result in the entire primary layer being constrained to the same tie-line.

Convection in the ternary alloy system is controlled first by the two independent Rayleigh numbers, but is also influenced by the base state properties such as mushy-layer thickness and permeability. The overall depth of the combined mushy layers is dependent primarily on the far-field temperature, while the relative thickness of each layer, as well as the permeability of each layer, is controlled mainly by the initial liquid compositions. An array of different base-state configurations were examined.

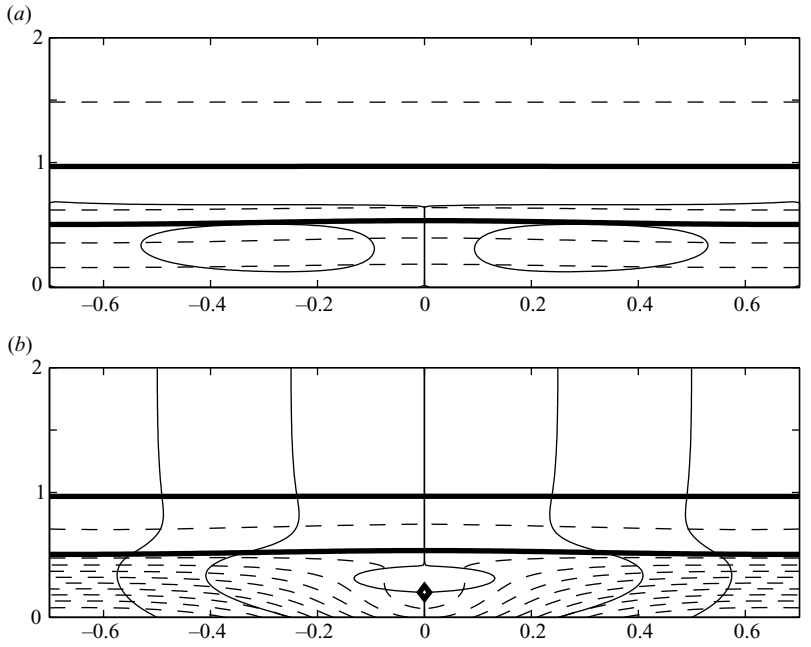

FIGURE 10. Nonlinear solutions for base case I(v). (*a*) Streamlines associated with the buoyant convection (solid curves using equal spacing of 0.1 between contours) and isotherms (dashed curves using equal spacing of 0.25 between contours). (*b*) Streamlines for the total mass flux (solid curves) and the total solid fraction (dashed curves using equal spacing of 0.02 between contours). The diamond shows the location of a primary mush inclusion in the secondary mushy layer.

For representative base states, our linear and nonlinear results documented convection in the ternary alloy system for cases in which: (i) the secondary layer was very stably stratified and the primary layer was unstably stratified, (ii) the secondary layer was neutrally stratified and the primary layer was unstably stratified, (iii) both layers were unstably stratified, (iv) the secondary layer was unstably stratified and the primary layer was neutrally stratified, and (v) the secondary layer was unstably stratified and the primary layer was very stably stratified.

The penetration of convection from an unstably stratified layer to a stably stratified layer was controlled by the strength and location of the unstable stratification and the permeability contrast between layers. Convection in the primary layer was found to generally induce a flow (comparable in magnitude) in the liquid layer, but only a weak flow in the secondary layer. This was particularly notable if the secondary layer had a much lower permeability. Convection in the secondary mushy layer, however, generally produced a significant flow in the primary and liquid layers unless the primary layer (which always had a higher average permeability than the secondary layer) was sufficiently stably stratified to effectively contain the convection within the secondary layer.

We found that a sharp stability contrast between primary and secondary layers leads to smaller-scale convection (in our calculations the smallest scale patterns were always associated with convection confined to a secondary layer by a very stably stratified primary mushy layer). It was in these cases where we observed 'stacked' convection cells. That is, with convection primarily localized in the unstable layer,

there was an adjacent set of rolls circulating in the opposite direction in the stably stratified layer. These stacked rolls were observed consistently in the linear solutions and the nonlinear solutions. Here we found that along a vertical line through both mushy layers, the solid fraction perturbation could be negative in one region and positive in another.

Our nonlinear calculations were consistent with our linear results, but also showed the further development of the flow at finite amplitude. As with its binary alloy counterpart, the ternary mushy-layer system is composed of reactive porous media whose solid matrix may undergo growth or dissolution as a result of transport of heat and solute by the flow. We have identified two manifestations of this property. First, for convection driven in the primary mushy layer, we found that nonlinear states with liquid inclusions in the primary mushy layer were possible. These inclusions are similar to those identified by Schulze & Worster (1999) for binary alloys. For convection driven in the secondary layer, we found that nonlinear states with primary mushy-layer inclusions in the secondary mushy layer (which is composed of dendrites of one species as well as dendrites of a second species) were possible.

While convection was found to be the result of a nearly vertical bifurcation over the range of amplitudes where the solid fractions remained positive, the nonlinear calculations revealed that the bifurcation for convection driven in the primary mushy layer was supercritical, and that driven in the secondary mushy layer was subcritical. Since the inclusion first develops where convection is the strongest, liquid inclusions in the primary layer were associated with supercritical bifurcations and mush inclusions in the secondary layer were associated with subcritical bifurcations. While this was true of all the cases we examined, including some not presented here, we emphasize that this correlation may not hold generally. This would be an interesting topic to explore with a weakly nonlinear analysis, which would allow for a computationally more efficient exploration of parameter space. A nonlinear stability analysis would also confirm that the subcritical solutions are unstable and the supercritical solutions stable, which is what we would anticipate from other convection problems. If this is indeed the case, the inclusions that form along a supercritical bifurcation could be studied experimentally – an option that is apparently unavailable for the binary system.

There are several additional avenues that warrant further investigation. First, there is the issue of modelling and calculating solutions with inclusions of primary mush in the secondary layer. This is a phenomenon unique to the ternary case and may be somewhat easier to capture than the liquid inclusions characteristic of the binary case since the governing equations are virtually the same on both sides of the interface. This situation would require a further generalization of the tie-line constraint so that each streamline entering such an inclusion would carry its own composition ratio for the passive species. Secondly, the inclusion of solutal diffusion (where the tie-line constraint does not apply) may reveal new convective modes not observed here. In particular, we anticipate that the inclusion of solutal diffusivity in the ternary case will lead to a second mode of fine-scale convection in the diffusive boundary layer at the liquid–mush interface analogous to that identified for binary convection by Worster (1992). In the ternary alloy, Anderson (2003) showed the existence of a solute boundary layer above the mush–mush interface and we may expect additional modes associated with this boundary layer. Finally, a detailed analysis of the effects of thermal convection in the ternary system, as was undertaken for binary alloys by Chen *et al.* (1994), as well as the effects of time dependence and three-dimensional geometry may be both tractable and of interest for ternary alloys.

The authors would like to acknowledge support from the 3M Non-Tenured Faculty Award Program (D.M.A.) and the National Science Foundation, DMS–0306996 (D.M.A.) and DMS–0405650 (T.P.S.). The authors would also like to thank G. B. McFadden and M. G. Worster for helpful discussions.

REFERENCES

Aitta, A., Huppert, H. E. & Worster, M. G. 2001*a* Diffusion-controlled solidification of a ternary melt from a cooled boundary. *J. Fluid Mech.* **432**, 201–217.

Aitta, A., Huppert, H. E. & Worster, M. G. 2001*b* Solidification in ternary systems. In *Interactive Dynamics of Convection and Solidification* (ed. P. Ehrhard, D. S. Riley & P. H. Steen), pp. 113–122. Kluwer.

Amberg, G. & Homsy, G. M. 1993 Nonlinear analysis of buoyant convection in binary solidification with application to channel formation. *J. Fluid Mech.* **252**, 79–98.

Anderson, D. M. 2003 A model for diffusion-controlled solidification of ternary alloys in mushy layers. *J. Fluid Mech.* **483**, 165–197.

Anderson, D. M. & Worster, M. G. 1995 Weakly nonlinear analysis of convection in mushy layers during the solidification of binary alloys *J. Fluid Mech.* **302**, 307–331.

Anderson, D. M. & Worster, M. G. 1996 A new oscillatory instability in a mushy layer during the solidification of binary alloys. *J. Fluid Mech.* **307**, 245–267.

Beckermann, C., Gu, J. P. & Boettinger, W. J. 2000 Development of a freckle predictor via Rayleigh number method for single-crystal nickel-base superalloy castings. *Metall. Mat. Trans.* A **31** 2545–2557.

Bloomfield, L. J. & Huppert, H. E. 2003 Solidification and convection of a ternary solution cooled from the side. *J. Fluid Mech.* **489**, 269–299.

Boettinger, W. J., Kattner, U. R., Coriell, S. R., Chang, Y. A. & Mueller, B. A. 1995 Development of multicomponent solidification micromodels using a thermodynamic phase diagram data base. In *Modeling of Casting, Welding and Advanced Solidification Process VII* (ed. M. Cross & J. Campbell) pp. 649–656. Warrendale, PA.

Chen, F., Lu, J. W. & Yang, T. L. 1994 Convective instability in ammonium chloride solution directionally solidified from below. *J. Fluid Mech.* **276**, 163–187.

Chung, C. A. & Chen, F. 2000 Onset of plume convection in musy layers. *J. Fluid Mech.* **408**, 53–82.

Chung, C. A. & Worster, M. G. 2002 Steady-state chimneys in a mushy layer. *J. Fluid Mech.* **455**, 387–411.

Davis, S. H. 2001 *Theory of Solidification.* Cambridge University Press.

Emms, P. W. & Fowler, A. C. 1994 Compositional convection in the solidification of binary alloys. *J. Fluid Mech.* **262**, 111–139.

Felicelli, S. D, Poirier, D. R. & Heinrich, J. C. 1997 Macrosegregation patterns in multicomponent Ni-base alloys. *J. Cryst. Growth* **177**, 145–161.

Felicelli, S. D, Poirier, D. R. & Heinrich, J. C. 1998 Modeling freckle formation in three dimensions during solidification of multicomponent alloys. *Metall. Mat. Trans.* B **29**, 847–855.

Krane, M. J. M. & Incropera, F. P. 1997 Solidification of ternary metal alloys–II. Prediction of convective phenomena and solidification behaviour of Pb–Sb–Sn alloys. *Intl J. Heat Mass Transfer* **40**, 3837–3847.

Krane, M. J. M., Incropera, F. P. & Gaskell, D. R. 1997 Solidification of ternary metal alloys–I. Model development. *Intl J. Heat Mass Transfer* **40**, 3827–3835.

Krane, M. J. M., Incropera, F. P. & Gaskell, D. R. 1998 Solidification of a ternary metal alloy: a comparison of experimental measurements and model predictions in a Pb–Sb–Sn system. *Metall. Mat. Trans.* A **29**, 843–853.

McKibbin, R. & O'Sullivan, M. J. 1980 Onset of convection in a layered porous medium heated from below. *J. Fluid Mech.* **96**, 375–393.

McKibbin, R. & O'Sullivan, M.J. 1981 Heat transfer in a layered porous medium heated from below. *J. Fluid Mech.* **111**, 141–173.

Nield, D. A & Bejan, A. 1999 *Convection in Porous Media*, 2nd. edn. Springer.

Riahi, D. N. 2002 On nonlinear convection in mushy layers. Part 1. Oscillatory modes of convection. *J. Fluid Mech.* **467**, 331–359.

Schneider M. C., Gu, J. P., Beckermann, C., Boettinger, W. J. & Kattner, U. R. 1997 Modeling of micro- and macrosegregation and freckle formation in single-crystal nickel-base superalloy directional solidification. *Metall. Mat. Trans.* A **28**, 1517–1531.

Schulze, T. P. & Worster, M. G. 1998 A numerical investigation of steady convection in mushy layers during the directional solidification of binary alloys. *J. Fluid Mech.* **356**, 199–220.

Schulze, T. P. & Worster, M. G. 1999 Weak convection, liquid inclusions and the formation of chimneys in mushy layers. *J. Fluid Mech.* **388**, 197–215.

Schulze, T. P. & Worster, M. G. 2001 Mushy zones with fully developed chimneys. In *Interactive Dynamics of Convection and Solidification* (ed. P. Ehrhard, D. S. Riley & P. H. Steen), pp. 71–80. Kluwer.

Schulze, T. P. & Worster, M. G. 2005 A time-dependent formulation of the mushy-zone-free boundary problem. *J. Fluid Mech.* **541**, 193–202.

Smallman, R. E. 1985 *Modern Physical Metallurgy*. Butterworths.

Thompson, A. F., Huppert, H. E. & Worster, M. G. 2003*a* A global conservation model for diffusion-controlled solidification of a ternary alloy. *J. Fluid Mech.* **483**, 191–197.

Thompson, A. F., Huppert, H. E., Worster, M. G. & Aitta, A. 2003*b* Solidification and compositional convection of a ternary alloy. *J. Fluid Mech.* **497**, 167–199.

Trefethen, L. N. 2000 *Spectral Methods in Matlab*. SIAM, Philadelphia.

Worster, M. G. 1986 Solidification of an alloy from a cooled boundary. *J. Fluid Mech.* **167**, 481–501.

Worster, M. G. 1992 Instabilities of the liquid and mushy regions during solidification of alloys. *J. Fluid Mech.* **237**, 649–669.

Worster, M. G. 1997 Convection in mushy layers. *Annu. Rev. Fluid Mech.* **29**, 91–122.

Worster, M. G. 2000 Solidification of Fluids. In *Perspectives in Fluid Dynamics* (ed. G. K. Batchelor, H. K. Moffatt & M. G. Worster), pp. 393–446. Cambridge University Press.